RESEARCH ARTICLE

Motion and elastic response of wind-tracing floating offshore wind turbines

Azin Lamei[1] · Masoud Hayatdavoodi[1,2] [iD] · H. Ronald Riggs[3]

Abstract

A multi-unit floating offshore wind turbine concept, the wind-tracing floating offshore wind turbine, is introduced. In this concept, the floating structure is a triangular platform that hosts three 5 MW wind turbines and is moored to the seabed with a turret-bearing mooring system. This mooring system allows the structure to rotate about the turret such that the total yaw moment by the environmental load on the turret is minimized. In this study, the optimum properties of the mooring lines and the location of the turret are determined. To identify the preferred location of the turret, the responses of the structure to combined co-directional and misaligned wind and wave loads are computed. The motions of the structure are obtained with a frequency-domain numerical model integrated with structural finite-element method for hydroelastic and aeroelastic analyses. The hydrodynamic and aerodynamic loads are obtained by wave diffraction theory and steady blade element momentum method, respectively. Finally, with the optimum configuration of the mooring system, the motion and aero- and hydroelastic responses of the fully flexible wind-tracing floating offshore wind turbines to combined waves and wind loads are determined and discussed.

Keywords Floating offshore wind turbines · Offshore wind · Turret-bearing mooring system · Wind-tracing

1 Introduction

Electrical power generated from the marine renewable energies reached up to approximately 43 GWh in 2016, with 97% of it due to offshore wind energy; see Weiss et al. (2018). Offshore wind installations are growing steadily, where by the end of 2021, the global cumulative offshore wind power capacity increased up to 56 GW, representing 7% of the total global cumulative wind installation; see Lee and Zhao (2022). Offshore wind is stronger and less turbulent and offers better wind energy potential to the wind industry developers than onshore sites. Thus, to access larger and more accessible wind speeds offshore, the wind industry has expanded from turbines with bottom-fixed foundations in shallow waters to floating offshore wind turbines (FOWTs) moored in deep waters; see Farr et al. (2021). With the promising growth of research and technology in offshore wind energy, numerous concepts regarding the rotor size and capacity, mooring layout, controller systems, and the substructures have been developed and studied. The single-unit platforms for FOWTs are namely single point anchor reservoir (SPARs) and semisubmersibles moored by catenary mooring lines and tensioned leg platforms (TLPs) connected to the seabed with taut cables.

There is a growing interest in the design and application of multi-unit platforms for FOWTs. In multi-unit FOWTs (MUFOWT), a single large substructure supports several wind turbines. The concept of MUFOWTs together with its challenges and advantages were discussed and analyzed in its early days by Barltrop (1993). The main advantage of the MUFOWT concept is that the cost of installation, marine operations and mooring systems for multiple units of wind turbines can be minimized, potentially.

The design of the platform and its mooring layout is of the main challenge of MUFOWTs. The distance between the rotors on the same platform should be large enough to reduce the rotor wake interaction of the front wind turbines with the

✉ Masoud Hayatdavoodi
  mhayatdavoodi@dundee.ac.uk

[1] Civil Engineering Department, School of Science and Engineering, University of Dundee, Dundee DD1 4HN, UK

[2] College of Shipbuilding Engineering, Harbin Engineering University, Harbin, China

[3] Civil and Environmental Engineering Department, University of Hawaii, Honolulu, HI 96822, USA

rear ones. To design such a system, an optimum number of the wind turbines should be considered to minimize the cost. The elastic behavior of floating platforms might play an important role in their motions due to their large characteristic lengths. Moreover, the addition of several wind turbines to the platform affects its structural responses. Thus, the hydroelastic behavior of the structure should be considered (in addition to the aeroelastic behavior of the turbine) for the design of the platform and its material properties.

To increase the power output of a FOWT, the weathervaning mechanism is introduced, which rotates the structure such that the wind turbines face the dominant incoming wind. The weathervaning of a MUFOWT depends mostly on its mooring system. The cost of the mooring lines is significant and their materials and layout should be determined accordingly. Turret-bearing mooring systems are largely applied for weathervaning applications of floating production storage and offloading vessels, and can be a possible option for MUFOWTs; see Zanganeh and Thiagarajan (2018), Huang et al. (2019) and Nair et al. (2019) among others. In this mooring layout, the platform is allowed to rotate about the turret in response to the combined effect of aerodynamic load on the rotors and the towers and hydrodynamic loads of the wave and current on the platform. Therefore, the moments on the structure due to the environmental loads are minimized. Moreover, independent controllers on each rotor of a FOWT improves the total power output of the system.

In a study by Henderson and Patel (2000), two optimized configurations for MUFOWT substructures with and without weathervaning mooring system were introduced. An H-shaped platform is designed for the non-weathervaning MUFOWT, where four towers are supported by the free-ends of the platform. For the weathervaning configuration, a V-shaped platform with three wind turbines at the vertex and its two free-ends was specified, moored with a turret bearing to the seabed. The turret-bearing in the latter configuration results in a more costly concept compared with the former designed MUFOWT.

Several other concepts have been developed similar to the weathervaning MUFOWT introduced by Henderson and Patel (2000). Commonly, a MUFOWT consists of a triangular platform and two or three wind turbines. The towers are supported by columns at the vertices of the substructure, and mooring cables connect the bottom of the columns to the seabed; see Ishihara et al. (2007b), Ishihara et al. (2007a), Hu et al. (2014) and Bae and Kim (2014) among others. Hanssen et al. (2015) introduced W2Power concept, a triangular platform hosting two wind turbines. In W2Power MUFOWT, the platform is moored with a turret-bearing mooring system and the towers are inclined to increase the spacing between the rotors. Furthermore, the wind-tracing FOWT was introduced by Wong (2015) with three wind turbines and a weathervaning mechanism by turret-bearing mooring

system. Preliminary analysis on its wave-induced responses and its motions to the combined wind and wave loads were reported by Lamei et al. (2019) and Li et al. (2019).

MUFOWTs are still in concept stage and a few studies have been carried out on modeling their responses to the environmental loads. Considering a general concept of a FOWT, the simultaneous effect of the environmental loads on the rotor, the tower, the platform and the mooring forces on the structure, results in their complex dynamics. The wind thrust force on the rotor and the wave loads on the platform are, respectively, the main aerodynamic and hydrodynamic load contributions on the global motion of a FOWT. Several numerical tools have been developed to model the FOWTs and predict their motions in response to various environmental loads. The aero-hydro-servo-elastic numerical tools are classified into fully coupled and decoupled numerical tools. The former approach models the coupling of the loads on the FOWT and its motions accurately by solving the governing equations of the domain (air and water) and the structure simultaneously, for instance computational fluid dynamics. In practice, to lessen the computational demand of fully coupled numerical tools, the structure is assumed to be rigid and its motions are restricted in a few degrees of freedom (DOF). The decoupled numerical approaches are based on independent solvers for aerodynamic and hydrodynamic loads on the structure. Moreover, the decoupled numerical tools offer faster simulations but assume that the motions of the structure are small and if elasticity is of interest, only the flexibility of the blades and the tower are considered. See Lamei and Hayatdavoodi (2020) for a recent review on the approaches used for aerodynamic, hydrodynamic and structural analyses of FOWTs.

Addition of multiple towers on a single platform and the specific mooring layout require a dedicated numerical coupling tool to analyze MUFOWTs. Moreover, the elasticity of a MUFOWT substructure might be significant and should be accounted in its load and motion analysis. To the authors' knowledge, there has not been any study with fully coupled numerical tools on the motions of a MUFOWT. However, a few studies have used decoupled numerical tools to analyze MUFOWTs. For instance, in an early study by Henderson and Patel (2000) and Henderson and Patel (2003), the aerodynamic and hydrodynamic loads on a MUFOWT were computed with steady-state blade element momentum method, and linear diffraction theory, respectively. This approach is developed for a fully rigid structure and the interaction of the rotor wakes is not considered. In this study, the loads and responses of a semisubmersible MUFOWT supporting five wind turbines was obtained and it was shown that the motions of the structure are mainly dominated by the inertial loads and the effect of the aerodynamic force on the motions of the structure are insignificant.

Later, Bae and Kim (2014) developed a coupling numerical tool for a MUFOWT with a triangular substructure. In this study, a numerical modeling tool for FOWTs, FAST (Jonkman et al. 2018), was further developed to account for the effect of several wind turbines placed on a single platform. FAST was linked to a time-domain solver, CHARM3D (Kim et al. 2001), to add the external forces by waves and current on the platform to the final equation of motion. Similar study by Bae and Kim (2015) was carried out on a semisubmersible MUFOWT with a trapezoidal shape, supporting five 5-MW wind turbines, in two arrays. The developed numerical tool in these studies neglect the rotor wake interactions of the front and rear wind turbines. Jang et al. (2015) and Kang et al. (2017) studied motions of a rigid and a flexible square semisubmersible MUFOWT, namely KRISO, under wind, wave and current loads using the coupled FAST-CHARM3D numerical tools. Regarding the responses of the flexible structure, a strong coupling between the substructure and the mooring lines was found in nonlinear waves. Moreover, a MUFOWT with six 8 MW rotors on a semisubmersible platform is introduced and studied by Bashetty and Ozcelik (2020c). The platform is a pentagonal structure and is moored with four catenary mooring lines all connected to a merging point at the center of the structure at one end. The hydrodynamic and aerodynamic loads on the structure are computed with a decoupled numerical approach based on linear diffraction wave theory and computational fluid dynamics calculations, respectively. See Bashetty and Ozcelik (2020a) and Bashetty and Ozcelik (2020b).

A numerical coupling approach was developed by Lamei et al. (2022) to model aero- and hydroelastic responses of a single-unit FOWT. In this approach, the aerodynamic load is computed with steady BEM and the wave interaction of the substructure is modeled with linear diffraction wave theory. The numerical tool is a potential-flow solver integrated with finite-element method, HYDRAN-XR (see NumSoft Technologies (2020)), which is enhanced to include a blade element momentum method (BEM) solver for aerodynamic analysis of FOWTs. For the present study, the numerical approach is further developed to model the motions of a MUFOWT. The theory on motion and load analysis of rigid and flexible FOWTs and the developed numerical approach are discussed in Sect. 2. Next, the wind-tracing FOWT together with its mooring line properties and configurations are introduced in Sect. 3. In Sect. 4, first, the environmental conditions that are considered for the aero- and hydroelastic analysis are described. Then, the motions of the rigid wind-tracing FOWT for different layouts of its mooring system to combined wind and wave loads are presented. For the optimum configuration of the turret-bearing mooring system, the rigid-body responses to wave loads and aero- and hydroelastic responses of the structure to combined wind and wave

loads are presented. Finally, further discussion about the elasticity behavior of the structure and its effects on its motions are provided.

2 Rigid- and flexible-body responses of a FOWT

A coupling numerical approach for hydroelastic and aeroelastic analyses of FOWTs was developed and introduced by Lamei et al. (2022). In this approach, the motions of a FOWT to the aerodynamic and hydrodynamic loads are obtained using linear diffraction wave theory and the blade element momentum method, respectively. The flexibility of the entire structure is accounted for by utilizing an integrated finite-element analysis module. The theory and the governing equations are presented and discussed in this section followed by introduction of the numerical tool, HYDRAN-XR, applied to obtain the elastic responses of FOWTs to combined wind and wave loads.

2.1 Hydrodynamic analysis

The environmental loads on a FOWT consists of aerodynamic and hydrodynamic loads, hydrostatic restoring forces and moments and the forces by the mooring lines. In the absence of the current, the hydrodynamic load on the structure is due to the hydrodynamic pressure and excitation forces and moments (sum of diffraction and Froude–Krylov forces).

An earth-fixed Cartesian coordinate system is chosen with the origin on the still water level (SWL), and z-axis pointing upwards; see Fig. 1. The translational motions, surge (ξ_1), sway (ξ_2), and heave (ξ_3), are parallel to the x-, y- and z-axes, respectively, and the rotational motions, roll (ξ_4), pitch (ξ_5), and yaw (ξ_6), are about the x-, y- and z-axes, respectively. Assuming that wave amplitude and the wave-induced motions and rotations of the structure are small and that viscous forces are negligible, the hydrodynamic loads and the wave interaction with the platform are obtained with linear diffraction wave theory. The fluid velocity is described by the velocity potential and Laplace's equation governs the domain. In linear wave theory, the total hydrodynamic load is determined by superpositioning the loads due to the added mass and hydrodynamic damping components, excitation forces and moments and the hydrostatic restoring terms. Here, the mooring forces are modeled linearly with a stiffness matrix. The motions of the structure in its rigid-body modes are obtained as

$$\xi_k \left[-\omega^2 \left(M_{jk} + a_{jk} \right) + i\,\omega\,b_{jk} + c_{jk,\text{hst}} + c_{jk,\text{moor}} \right]$$
$$= A\,X_j, \quad j, k = 1, 2, \ldots, 6, \tag{1}$$

Fig. 1 **a** Schematic of the wind-tracing FOWT and **b** characteristic dimensions of the wind-tracing FOWT

(a)

(b)
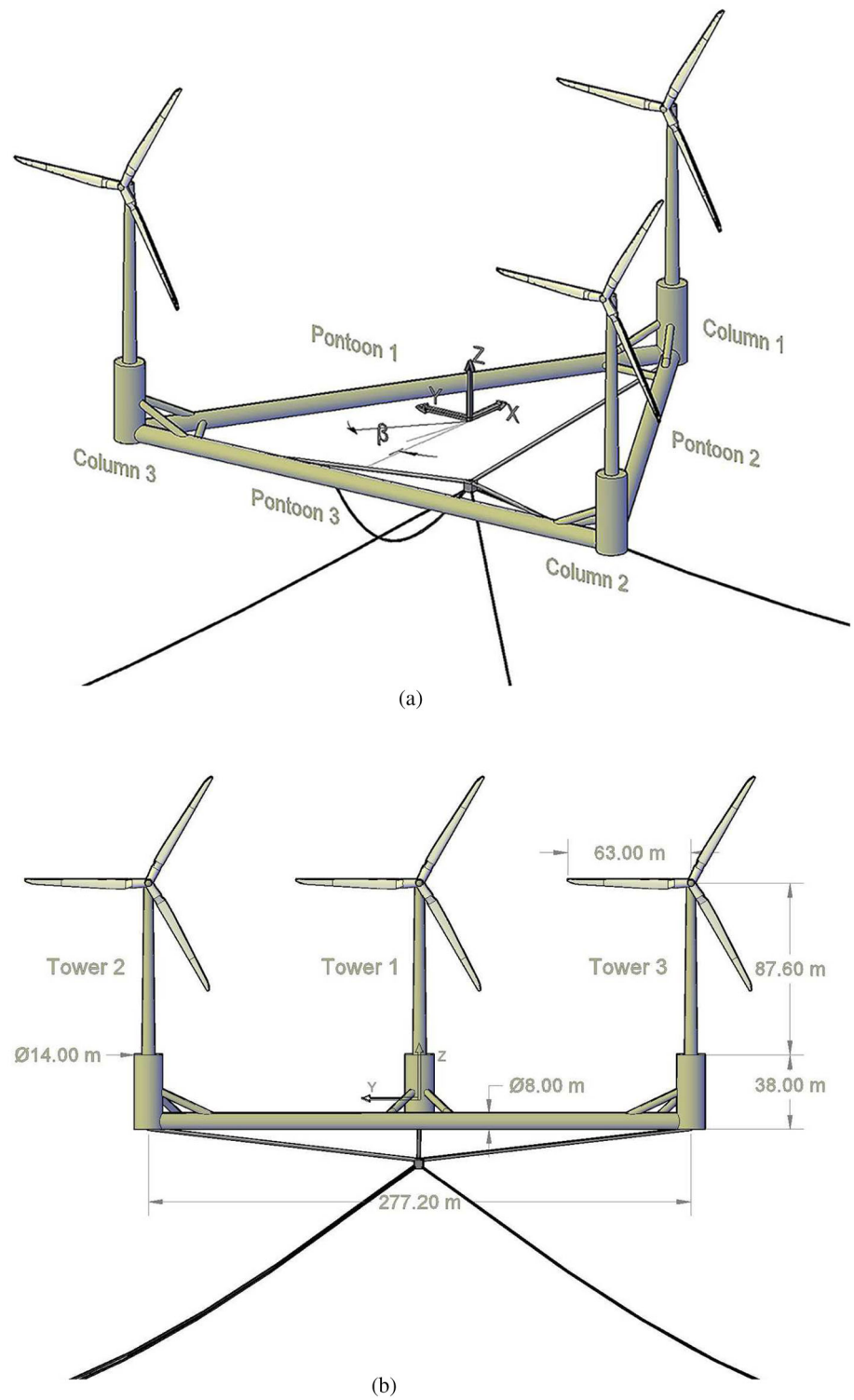
where ω is the wave frequency, M_{jk} is the linearized body inertia mass matrix, ξ_k is the complex body response phasor in mode k and $i = \sqrt{-1}$. Moreover, a_{jk} and b_{jk} are the added mass and hydrodynamic damping coefficients, and $c_{jk,\mathrm{hst}}$ and $c_{jk,\mathrm{moor}}$ are the hydrostatic restoring and mooring stiffness coefficients, respectively. A is the wave amplitude and X_j is the complex unit-amplitude of the exciting forces and moments in mode j, i.e., $F_{\mathrm{exciting}} = A\,X_j$.

2.2 Aerodynamic analysis

The aerodynamic load on the rotor is computed with steady blade element momentum method (BEM). Air is assumed to be incompressible and inviscid and the incoming airflow is axisymmetric with respect to the rotor. The rotor is considered as an impermeable disk (with an infinite number of blades), discretized into annular control volumes. The governing equations in BEM are based on the conservation of mass and the axial and angular momentum balances and are satisfied at each control volume along the blades.

For each control volume on the rotor, the normal and tangential forces produced by the incoming wind are by empirical relations for the drag and lift forces. Given that the aerofoil shape is now commonly used for the turbine blades, the empirical coefficients of drag and lift forces are tabulated. These coefficients are obtained experimentally as a function of the angle of attack and the Reynolds number of the incoming wind speed. The sum of the tangential and the normal forces on the blades result in the torque on the rotor shaft and the thrust force acting at the hub center of the rotor, respectively. The thrust force, T, is computed as

$$T = \frac{1}{2}\rho_a A_r C_T V_0^2, \tag{2}$$

where ρ_a and A_r are the air density and the rotor projected area, respectively, V_0 is the incoming wind speed to the rotor and C_T is the thrust coefficient.

To determine the motions of a FOWT under combined wind and wave loads in frequency domain, the total aerodynamic load on the structure is linearized with a harmonic function. It is assumed that the wind thrust force on a fixed rotor acts as an excitation force in the wind propagation direction and with the same frequency as the incoming waves. This assumption is made to allow for addition of the wind load to the equation of motion of the structure. See Kvittem and Moan (2014), Wang et al. (2016) and Lamei et al. (2022) for discussion about applicability and limitations of this assumption to this problem. Hence, the harmonic aerodynamic force, $F_{j,W}$, at the tower top is given as

$$F_{j,W} = |F_{j,W}|\cos(\omega t - \delta_{\mathrm{aero}}), \quad j = 1, 2, \ldots, 6, \tag{3}$$

where δ_{aero} is the phase angle of the aerodynamic force. Given that the towers are always circular cylinders and the wind load is assumed harmonic with frequency ω, the aerodynamic load phase angle is determined following the same analytical relations developed by MacCamy and Fuchs (1954) for wave interactions with a fixed circular cylinder. Therefore, δ_{aero} is determined as

$$\delta_{\mathrm{aero}}(kr_0) = \tan^{-1}\left[\frac{Y_1'(kr_0)}{J_1'(kr_0)}\right], \tag{4}$$

where $J_p'(kr)$ and $Y_p'(kr)$ are the derivatives of $J_p(kr)$ and $Y_P(kr)$, the Bessel functions of the first kind and the second kind of order p, respectively, and r_0 is the top diameter of the tower. Substituting Eq. (2) into Eq. (3) gives the harmonic aerodynamic force on a fixed rotor, i.e.,

$$F_{1,W} = \frac{1}{2}C_T\rho_a V_0^2 A_r \cos(\omega t - \delta_{\mathrm{aero}}). \tag{5}$$

Given the motion of the floating structure, the thrust force is computed with respect to the relative incoming wind speed to the rotor. Assuming that the incoming wind direction is always horizontal and orthogonal to the rotor, only the motions of the structure in x-direction contribute to relative incoming wind speed. Therefore Eq. (2) is solved for $V_{\mathrm{rel}} = V_0 - \dot{x}$ where V_{rel} and $\dot{x}$ are the relative incoming wind speed to the rotor and the speed of the structure at the hub along the direction of the incoming wind. Assuming $\dot{x}$ is small, the thrust force on the rotor of a FOWT can be expressed as

$$T(V_{\mathrm{rel}}) = T(V_0) - \dot{x}\,\frac{\partial T(V_0)}{\partial V_0} + O(\dot{x}^2) + \cdots, \tag{6}$$

where the first term is the thrust force on a fixed rotor, given by Eqs. (2) and (5), and the second term is a function of both incoming wind speed and the speed of the structure at the hub center, representing the aerodynamic damping effect of the operating rotor. Furthermore, in Eq. (6), the terms containing $\dot{x}^2$ and higher orders are neglected. In frequency domain, the velocity of the structure at the hub in surge is given as $i\omega(\xi_1 + \xi_5(z_h - z_{cg}))$ where z_h and z_{cg} are the vertical coordinates of the hub center and the center of gravity of the complete system, respectively. Moreover, the partial derivative in the second term in Eq. (6) is obtained with respect to Eq. (2). Hence, Eq. (6) is rewritten as

$$T(V_{\mathrm{rel}}) = F_{1,W} - i\omega(\xi_1 + \xi_5(z_h - z_{cg}))B_{\mathrm{aero}}, \tag{7}$$

where $B_{\mathrm{aero}} = \rho_a C_T A_r V_0$ is the aerodynamic damping coefficient of the rotor.

The total aerodynamic load vector on a FOWT consists of the thrust force on the rotor in surge and its induced moments

about y and z-axes, respectively. In this approach, the effect of the front towers on the rear ones is assumed negligible. Hence, for a single- or a multi-unit FOWT with six degrees of freedom and its center of gravity in an arbitrary location, $C_G = (x_{cg}, y_{cg}, z_{cg})$, the aerodynamic load vector, F_W, is given as

$$
F_W = \begin{bmatrix} \sum_{j=1}^{n} |F_{1,W}^j| \cos(\omega t - \delta_{\text{aero}}^j) \\ 0 \\ 0 \\ 0 \\ -\sum_{j=1}^{n} |F_{1,W}^j| \times (z_h^j - z_{cg}) \cos(\omega t - \delta_{\text{aero}}^j) \\ -\sum_{j=1}^{n} |F_{1,W}^j| \times (y_h^j - y_{cg}) \cos(\omega t - \delta_{\text{aero}}^j) \end{bmatrix}, \quad (8)
$$

where n is the number of wind turbines installed on a single platform and $(x_h^{(j)}, y_h^{(j)}, z_h^{(j)})$ are the hub coordinates of rotor j. Furthermore, it is assumed that the thrust force and its aerodynamic damping effect in surge is significantly larger than in sway direction. The damping effect in sway is negligible due to steady BEM and hence in the aerodynamic damping matrix, only the terms in surge, the rotational modes of the structure and their coupling components with surge are nonzero:

$$
B_{jk,\text{aero}} = \begin{bmatrix} n \times (\rho_a C_T A_r V_0) & 0\ 0\ 0 & -\sum_{j=1}^{n} \rho_a C_T A_r V_0(z_h^j - z_{cg}) & -\sum_{j=1}^{n} \rho_a C_T A_r V_0(y_h^j - y_{cg}) \\ 0 & 0\ 0\ 0 & 0 & 0 \\ 0 & 0\ 0\ 0 & 0 & 0 \\ 0 & 0\ 0\ 0 & 0 & 0 \\ -\sum_{j=1}^{n} \rho_a C_T A_r V_0(z_h^j - z_{cg}) & 0\ 0\ 0 & \sum_{j=1}^{n} \rho_a C_T A_r V_0(z_h^j - z_{cg})^2 & 0 \\ -\sum_{j=1}^{n} \rho_a C_T A_r V_0(y_h^j - y_{cg}) & 0\ 0\ 0 & 0 & \sum_{j=1}^{n} \rho_a C_T A_r V_0(y_h^j - y_{cg})^2 \end{bmatrix}, \quad (9)
$$

where $B_{jk,\text{aero}}$ in rotational modes contains the effect of the offsets of the hub center from the center of gravity.

Given that the thrust force and the aerodynamic damping effect on a FOWT are harmonic, with frequency ω, the forces and moments of waves and wind are added linearly. Therefore, to obtain the motions of the structure to combined wind and wave loads, the aerodynamic load vector, Eq. (8), and its damping effect, Eq. (9), are added to the right- and left-hand side of Eq. (1), respectively, and the complete equation of motion reads

$$
\frac{\xi_k}{A} \left[-\omega^2 (M_{jk} + a_{jk}) + i\omega \left(b_{jk} + \frac{B_{jk,\text{aero}}}{A} \right) \right.
$$
$$
\left. + c_{jk,\text{hst}} + c_{jk,\text{moor}} \right] = X_j + \frac{F_{j,W}}{A},
$$
$$
j, k = 1, 2, \ldots, 6. \quad (10)
$$

The response amplitude operators (RAOs) of a FOWT to combined wind and wave loads, $\frac{|\xi_k|}{A}$, are determined by solving Eq. (10) at frequency ω. We will discuss the solution approach in the following sections.

2.3 Aero- and hydroelasticity analyses of FOWTs

Structural deformations of a flexible FOWT are obtained with a reduced basis approach. In this method, the deformations of the structure are presented with a linear superposition of mathematical mode-shapes determined with finite-element method. For a fully flexible FOWT, to account for the flexibility effects of the wind turbines and their supporting platform, a subset of m dry modes from the total possible modes of the flexible structure, N, are considered. These mode-shapes are sufficiently general to model the motions of the structure and are added as generalized modes to the total degrees of freedom of the rigid structure.

Therefore, the linearized frequency-domain analysis of fully flexible FOWTs is carried out for the rigid-body modes together with the generalized modes of the structure, representing the elasticity effects of the FOWT. In this case, the first six translational and rotational modes and the generalized modes are normalized by unit-displacements and unit-mass, respectively.

For a flexible floating structure, the hydrostatic restoring coefficients depend on both the change of hydrostatic pressure as external forces and internal stresses. Huang and Riggs (2000) obtained an explicit formulation of hydrostatic restoring coefficients by linearizing the internal and external forces and moments on the floating structure. Following this

approach, the complete formulation accounting for contributions of both internal stresses, c^g and hydrostatic pressure, c^f, is given by

$$c_{\text{hst}} = c^f + c^g, \tag{11}$$

and the complete hydrostatic restoring coefficient, $c_{ij,\text{hst}}$ is computed as

$$
\begin{aligned}
c_{ij,\text{hst}} = &-\rho_w g \int_{S_b} \psi_k^i (\psi_3^j + z\,\varepsilon_\nu^j)\, n_k \, \mathrm{d}S \\
&+ \rho_w g \int_{S_b} z \psi_l^i \, \psi_{k,l}^j \, n_k \, \mathrm{d}S \\
&+ \int_{\Omega_s} \sigma_{lm} \psi_{k,l}^i \psi_{k,m}^j \, n_k \mathrm{d}\Omega, \\
&q,l,m = 1,2,3, \quad i,j = 1,2,\ldots,m,
\end{aligned}
\tag{12}
$$

where ρ_w is the mass density of water, and S_b is the wetted surface. ψ_k^i is the displacement of k component in mode i, and $\psi_{k,l}^i$ is the partial derivative of the displacement of k component in mode i with respect to mode l, where i and l represent both rigid-body modes and the deformational generalized modes. n_k is the kth component of the normal vector on the wet surface. Ω_s is the structural volume, σ_{lm} is the structural stress under gravitational loads in calm seas, ϵ_ν^j is the volumetric strain in mode j. In Eq. (12), the first two integrals present the hydrostatic pressure and the last one represents the internal stresses.

For a flexible FOWT, the equation of motion is obtained by adding the generalized modes to the rigid-body equation of motion, Eq. (10),

$$
\begin{aligned}
\frac{\xi_k}{A} &\left[-\omega^2 (M_{jk} + a_{jk}) + \mathrm{i}\omega(b_{jk} + B_{jk,\text{aero}}) \right. \\
&\left. + c_{jk,\text{hst}} + c_{jk,\text{moor}} \right] = X_j + \frac{F_{j,W}}{A}, \\
&j,k = 1,2,\ldots,6,7,\ldots,m,
\end{aligned}
\tag{13}
$$

where the hydrostatic coefficient, $c_{jk,hst}$ is computed by Eq. (13) and m is the total number of modes of the FOWT.

2.4 Numerical model

The governing equations of aero- and hydroelastic analyses of a FOWT are derived and discussed in previous subsections. The numerical solution to this problem is obtained in HYDRAN-XR (NumSoft Technologies 2020), a potential-flow solver for hydrodynamic analysis, integrated with finite-element method for structural considerations. HYDRAN-XR is enhanced to include the blade element momentum method solver for aerodynamic analysis of the wind tur-

bines. The algorithm of integrated modules in HYDRAN-XR for aerodynamic, hydrodynamic and structural analyses are described in Lamei et al. (2022) and introduced briefly in the following discussion.

The mass and stiffness matrices, and the mode-shapes of a FOWT are computed with finite-element method. The structure is modeled with shell elements, where the rotor-nacelle-assembly is defined with distributed mass points at the top of the tower. The generalized modes, mass and stiffness matrices are obtained by specifying the material properties and thickness of the shell elements over the structure. Once the mode-shapes are obtained, the displacement of the structure is determined by a linear superposition of translational and rotational modes and the generalized modes due to the flexibility effects of the structure.

The aerodynamic analysis module in HYDRAN-XR considers the wind load on both the rotor and the tower. The aerodynamic normal forces and damping coefficients on the rotor are computed with BEM and distributed over the front face of the blades. For this purpose the nodes at each control volume facing the incoming wind flow are identified. The wind load on the tower is computed as

$$F_D = \frac{1}{2} C_d A V_0^2, \tag{14}$$

where $C_d = C_{d(\text{Re})}$ is the drag coefficient with respect to the incoming wind Reynolds number, $\text{Re} = \dfrac{V_0 D}{\nu}$, where D is the diameter of the tower, and ν is the kinematic viscosity of air at $20°$, and A is the cross sectional area of the tower. In this approach, the effect of the tower on the blades is assumed negligible. Similar to the rotor, the drag forces by the incoming wind on the tower are distributed over the nodes facing the wind. Here, the normal aerodynamic forces, and damping coefficients are applied as nodal forces and dampers on the selected nodes of the finite-element model.

For hydrodynamic analysis of the substructure, the finite element model is conformed to a panel mesh with a one-to-one mapping over the wet surfaces of the platform. The diffraction and radiation problem over the wet panels are solved with a three-dimensional source distribution, Green function method. Here, the square matrices of frequency-dependent hydrodynamic coefficients and the wave exciting forces for the rigid-body and the generalized modes are computed. Hence, with the mass and stiffness matrices obtained by finite-element method, and the total aerodynamic load vector and aerodynamic damping coefficients matrix, the governing equation of motion for combined wind and wave loads, Eq. (13) is solved for m modes. The responses of the structure are computed with a standard matrix solver in frequency domain as a function of frequencies ω.

3 Multi-unit wind-tracing floating offshore wind turbines

The primary concept of the wind-tracing FOWT is introduced and described by Wong (2015). Here, the characteristics and the properties of the wind-tracing FOWT together with the configuration of its mooring system are presented and discussed.

The wind-tracing platform consists of three columns and three pontoons, forming an equilateral triangular platform, shown in Fig. 1a. The columns and the pontoons are connected at the corners of the triangle with three braces. Each column has a diameter of 14 m and it is 38 m long from its end up to the bottom of the towers, supporting a 5 MW wind turbine. To reduce the interaction of the wakes downstream the rotors, the centers of the columns are $2.2D_r$ apart, where D_r is the diameter of the rotor. For a standard 5 MW wind turbine by national renewable energy laboratory (see Jonkman et al. (2009)), $D_r = 126$ m and hence the distance between the columns is 277.2 m. The pontoons are 264.2 m long with 8 m diameter, shown in Fig. 1b. Both the columns and the pontoons are made of prestressed concrete with 2400 kg/m^3 density, elasticity modulus of 35 GPa, and 0.2 Poison's ratio. The columns and the pontoons have a wall thicknesses of 0.4 m, and 0.35 m, respectively. The braces of the platform are made of steel, with 1.5 m in diameter and a wall thickness of 0.0175 m. The density of the steel braces is 7800 kg/m^3, with 210 GPa elasticity modulus and 0.3 Poison's ratio.

The wind-tracing FOWT is designed for deep waters with 200 m water depth, and 16 m draft. The structure is ballasted with water in both the columns and the pontoons. The ballast is added to each column such that under the hydrostatic equilibrium, the column floats at 16 m draft (if considered as a stand-alone floating object). The remainder of the ballast is distributed inside the three pontoons equally. The ballast distribution is given in Table 1.

The wind-tracing FOWT is moored to the seabed with a turret-bearing mooring system. The turret allows the structure to rotate to the direction of the dominant environmental loading to minimize the loads on the structure. A submerged turret below the pontoons is connected to the bottom of the columns with three taut cables. The turret is a $2 \times 2 \times 2$ m^3 steel cube. The taut cables are connected to a universal joint on the top surface of the turret, enabling the platform to rotate about the z-axis freely. Four catenary mooring lines connect the seabed to the bottom four corners of the turret, restricting the turret such that it can only rotate about its z-axis.

The properties of the taut cables and the catenary mooring lines are obtained with respect to the static equilibrium of the structure in the absence of the incoming waves and the wind loads. Shown in Fig. 2, the complete structure is in static equilibrium such that the total forces and moments on the structure by the taut cables are zero, i.e.,

Table 1 The mass distribution of the wind-tracing FOWT

Item	Value
Total weight of the full structure	230,986 ton
Total weight of the turret	643 ton
Ballast weight	237176 ton
Displaced volume	4.7001×10^4 m^3
Center of gravity (CG)	7.60 m below SWL
Center of buoyancy (CB)	11.2 m below SWL
Roll inertia about CG	3.55×10^{11} kg m^2
Pitch inertia about CG	3.58×10^{11} kg m^2
Yaw inertia about CG	6.85×10^{11} kg m^2

$$\sum F_x = -T_1 \cos\theta_1 + T_2 \cos\theta_2 \cos\alpha$$
$$+ T_3 \cos\theta_2 \cos(-\alpha) = 0, \tag{15}$$

$$\sum F_y = T_2 \cos\theta_2 \sin\alpha + T_3 \cos\theta_2 \sin(-\alpha) = 0, \tag{16}$$

$$\sum F_z = T_1 \sin\theta_1 + T_2 \sin\theta_2 + T_3 \sin\theta_2 = \rho_w \nabla_{wt} g$$
$$- M_{tot} g, \tag{17}$$

$$\sum M_x = T_2 \cos\theta_2 \sin\alpha (z_c - z_{cg})$$
$$- T_3 \cos\theta_2 \sin\alpha (z_c - z_{cg})$$
$$+ T_2 \sin\theta_2 \, y_c - T_3 \sin\theta_2 \, y_c = 0, \tag{18}$$

$$\sum M_y = T_2 \sin\theta_2 \, L_2 + T_2 \sin\theta_2 \, L_2 - T_1 \sin\theta_1 \, L_1$$
$$+ T_2 \cos\theta_2 \cos\alpha (z_c - z_{cg})$$
$$+ T_3 \cos\theta_2 \cos\alpha (z_c - z_{cg})$$
$$- T_1 \cos\theta_1 \cos\alpha (z_c - z_{cg}) = 0, \tag{19}$$

$$\sum M_z = T_2 \cos\theta_2 \sin\alpha \, y_c - T_3 \cos\theta_2 \sin\alpha \, y_c$$
$$+ T_2 \cos\theta_2 \sin\alpha \, L_2$$
$$- T_3 \cos\theta_2 \sin\alpha \, L_2 = 0, \tag{20}$$

where T_1, T_2 and T_3 are the pretension forces of cables 1, 2 and 3, respectively, and θ_1 and θ_2 are the angles of cables 1, and 2 and 3 with the horizontal plane, respectively. Moreover, M_{tot} is the total mass of the complete structure including the ballast inside the pontoons and ∇_{wt} is the displaced volume by the wind-tracing FOWT at 16 m draft. Since the platform is an equilateral triangle, cable 1 is always along the horizontal symmetry line and cables 2 and 3 are with angles α and $-\alpha$ with respect to the x-axis; see Fig. 2a, b. Moreover, z_c is the vertical component of taut cables fairleads at the bottom of the columns, y_c is the distance between the fairlead of cables 2 and 3 from the x-axis and L_1 and L_2 represent the horizontal distance between the center of gravity and the rear and front column, respectively.

The properties of the taut cables and the catenary mooring lines are extracted from an industrial product catalogue

Fig. 2 a The depths of the turret and **b** the horizontal locations of the turret

(a)

(b)
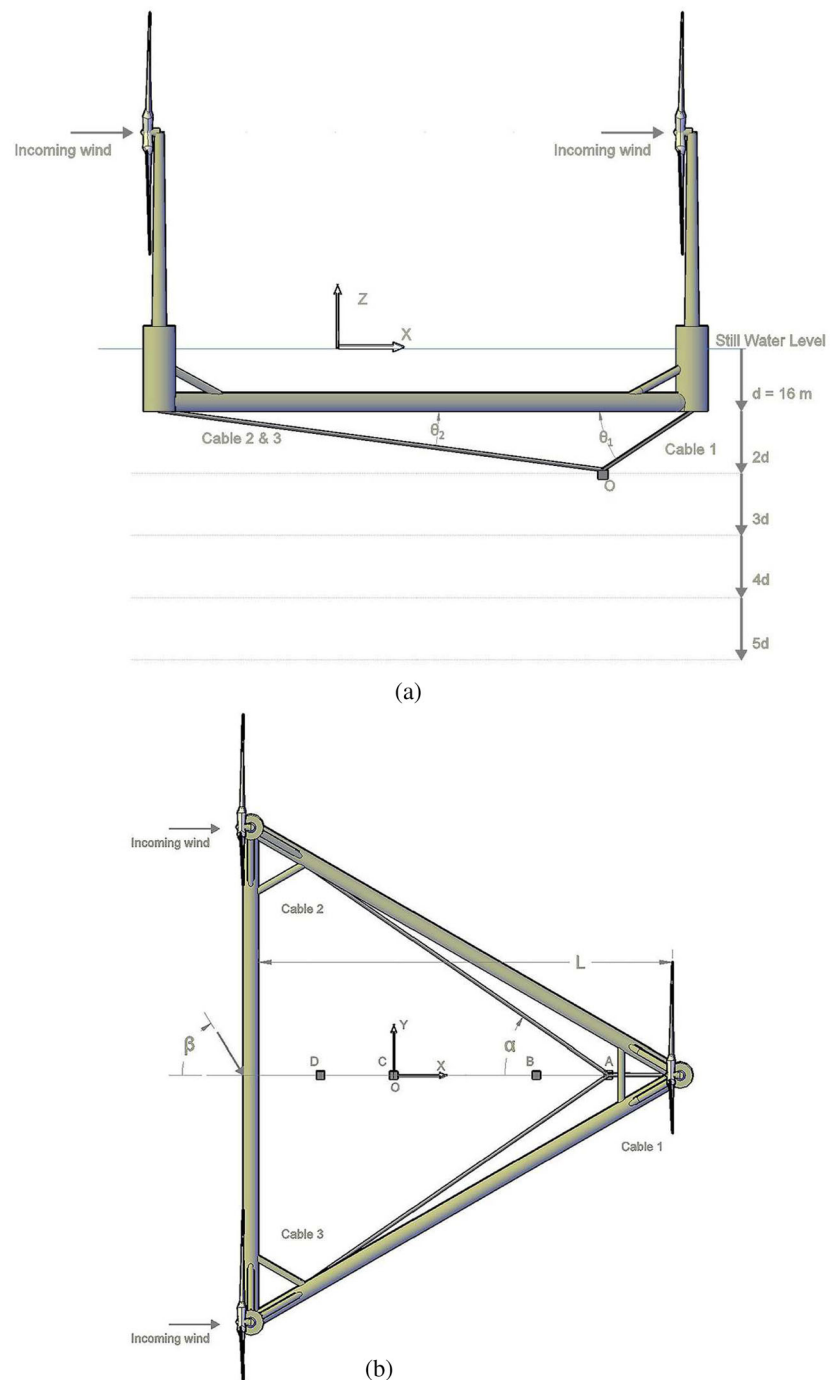
by Global Maritime Moorlink (2016). The required ballast and pretension forces of the taut cables are computed for $0° < \alpha < 60°$ and $0° < \theta_1 < 90°$. The variation of the two angles results in the change of the horizontal and vertical position of the turret under the equilibrium condition. In Eq. (17), for each α and β, the pretension forces of the cables are determined such that the contribution of the ballast in vertical equilibrium of the complete structure is minimized. Therefore, the properties assigned to the taut cables are cor-

responding to the maximum axial stiffness that is available in the industrial catalogue. The total pretension forces of the taut cables are obtained with respect to industrial standards provided by DNV (Det Norske Veritas) (2015). The minimum ballast that results in maximum pretension forces by the taut cables for $0° < \alpha < 60°$ and $0° < \theta_1 < 90°$ is identified.

The turret is neutrally buoyant and the vertical component of the total pretension force by the taut cables is equal to the

Table 2 The properties of the taut cables and the catenary lines of the wind-tracing FOWT

Item	Value
Taut diameter	153 mm
Taut axial stiffness	1481 MN/m
Catenary diameter	95 mm
Catenary wet weight	1942.4 N

total vertical pretension force by the catenary lines. Given the total vertical pretension force by taut cables, the properties of the catenary lines are obtained. It is assumed that the catenary mooring lines are identical and their pretension forces are only in vertical direction. As a result, spiral strand wire ropes with 153 mm diameter and R5 studless chains with 95 mm diameter are chosen for the taut cables and the catenary lines, respectively. The mass distribution of the wind-tracing FOWT and the details of its mooring lines are presented in Tables 1 and 2, respectively.

4 Results and discussion

In this section, first the environmental conditions that are considered for rigid- and flexible-body analyses of the wind-tracing FOWT are described. Next, the rigid-body responses of the structure to combined wind and wave loads are compared for several locations of the turret and the optimum layout of the mooring system is identified. These are followed by aero- and hydroelastic analyses of the structure to combined wind and wave loads.

The wind-tracing triangular platform and the three 5 MW wind turbines are modeled with shell elements; see Fig. 3. The center of gravity and the mass distribution of the complete structure are obtained using the finite-element analysis tool of HYDRAN-XR. Shown in Fig. 4, mesh convergence study for the freely floating (no mooring attached) wind-tracing FOWT floating at 16 m draft is performed with fine, medium and coarse panel sizes, namely 1.6 m, 2 m and 2.6 m. In all the three cases, the panel size on the braces is kept constant at 0.8 m. It is observed that the medium-sized panel (2 m) provides converged results. The magnitudes of the peaks are not meaningful as it is expected that they would be reduced substantially by damping. The simulation time for the converged mesh with 9768 panels is approximately 13 h on a desktop machine with Intel Core i5 6500, 3.20 GHz CPU and 16 GB memory.

4.1 Environmental conditions

In this study, the water depth is set to 200 m uniformly for the entire domain. The incoming waves are linear with unit wave

Fig. 3 The shell elements of the wind-tracing FOWT and the turret
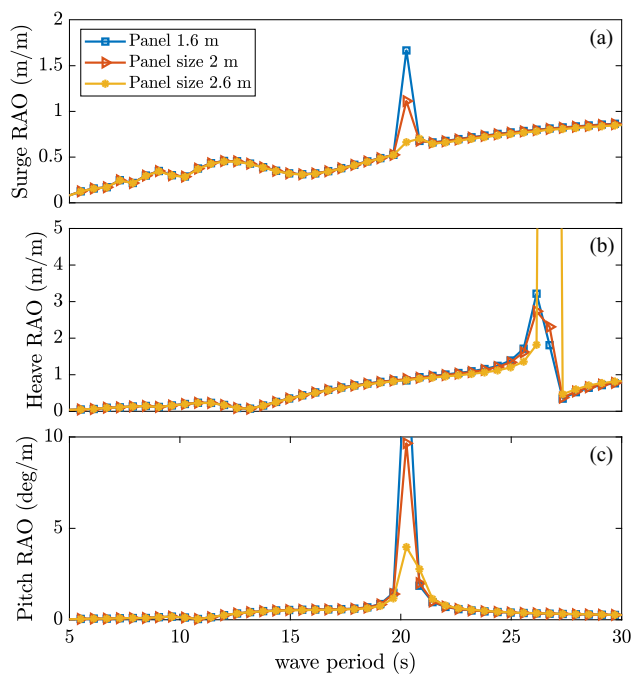
Fig. 4 Comparison of the head seas wave-induced RAOs of the freely floating rigid wind-tracing FOWT with three panels sizes, 1.6 m, 2 m and 2.6 m

amplitude and wave periods varying from 5 s to 30 s. Here, the contribution of the current loads on the floating platform and the submerged turret is neglected. Only one incoming wind speed is considered and the aerodynamic load on the three 5 MW wind turbines is obtained at their maximum power output, with steady wind speed of 11.4 m/s; see Jonkman et al. (2009).

For wave-induced responses of the wind-tracing structure (in the absence of wind), due to the symmetry of the triangular floating platform, only wave heading angles up to $\beta = 30°$ are considered. Furthermore, the incoming wave direction changes from $\beta = 0°$ to $\beta = 180°$; see Fig. 2b, for the
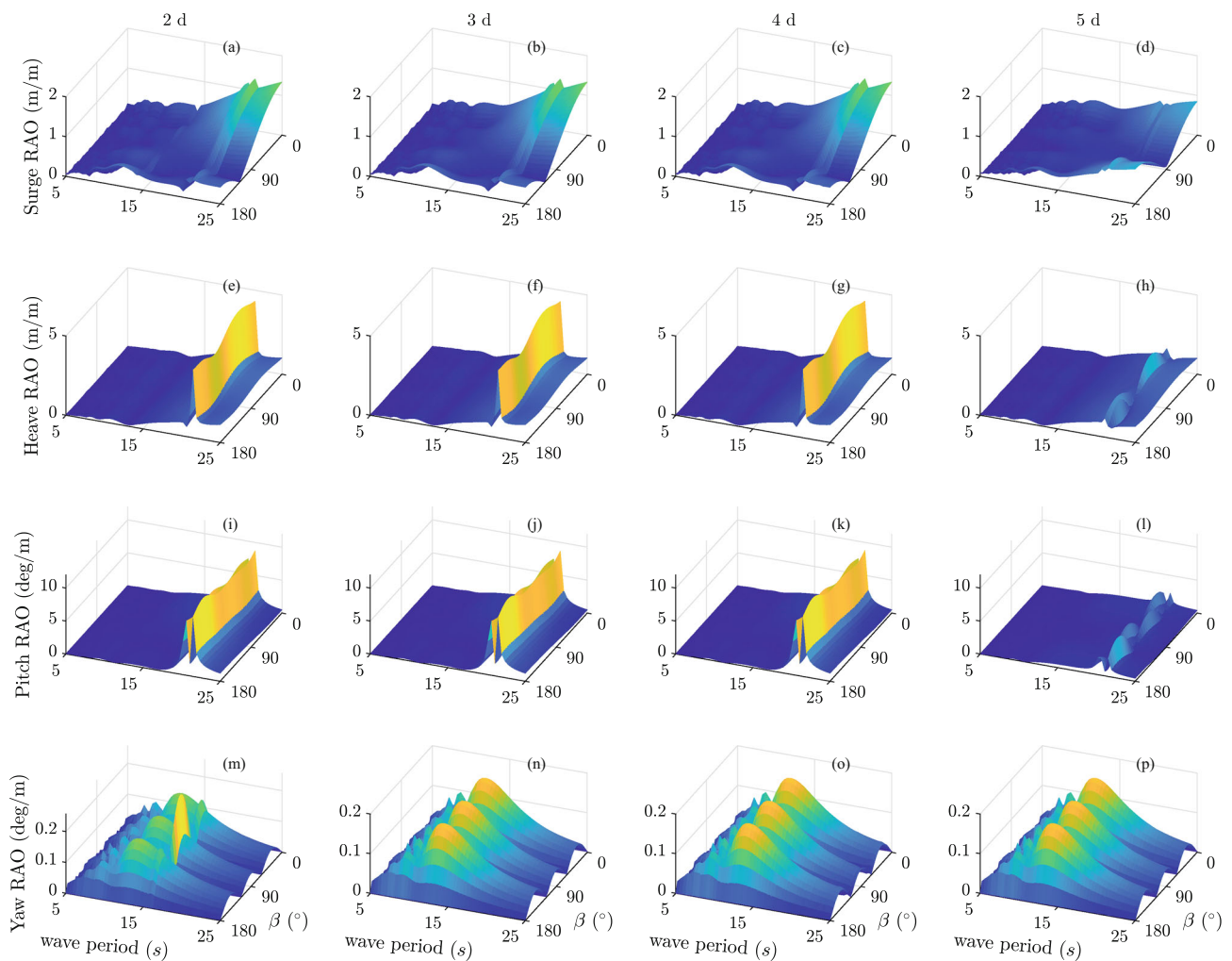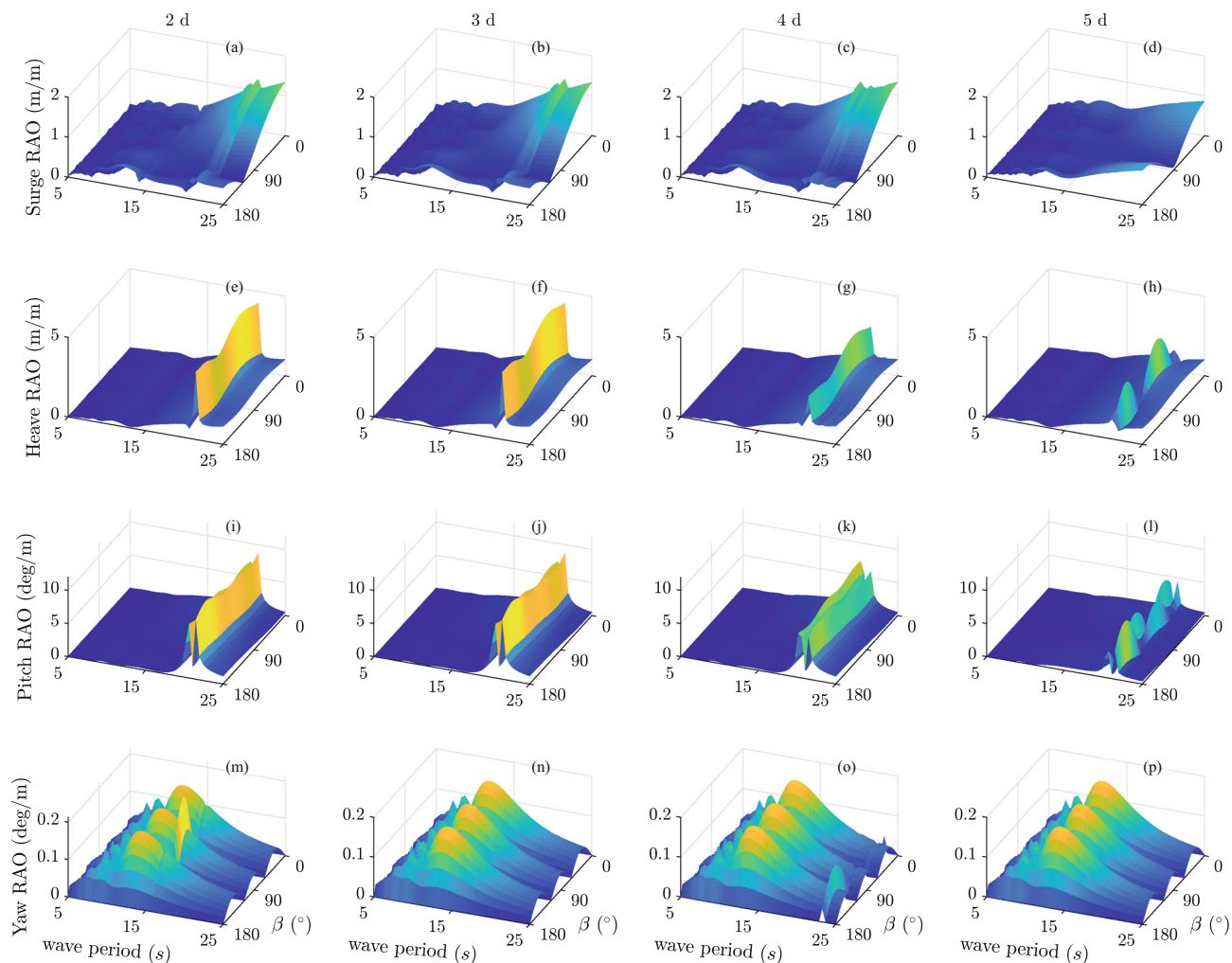
Fig. 5 Surge, heave, pitch and yaw RAOs of the wind-tracing FOWT to combined wind and wave loads for four depths of the turret at location A. Figure in color online

motions of the structure to combined wind and wave loads. Although, the aforementioned setting does not describe a complete environmental conditions, it allows us to evaluate the stability of the wind-tracing FOWT for co-directional and misaligned wind and wave loads.

4.2 Turret-bearing mooring configuration

As discussed in Sect. 3, by varying α and θ_1 shown in Fig. 2a, b, the turret can be in an infinite number of horizontal and vertical locations below the platform. In this study, the mooring configuration is limited to 16 possible locations for the turret. Shown in Fig. 2a, b, the turret can be at four horizontal locations, points A, B, C and D, where point C is along the vertical line passing through the center of gravity. The location of points A, B, C and D are chosen such that their distances from column 1 are $1/6L$, $2/6L$, $4/6L$ and $5/6L$, respectively where L is the horizontal distance between col-

umn 1 and pontoon 3. In the vertical direction, the depth of the turret can be at $2d$, $3d$, $4d$ or $5d$, where d represents the draft of the platform, 16 m. For each layout of the mooring system, the responses of the structure to co-directional and misaligned wind and wave loads are obtained. The incoming wind flow is always orthogonal to the rotor. Hence, to model the wind-wave misalignment, the wave heading angle changes.

The optimum configuration of the mooring system is chosen with the following steps: first, for each horizontal location of the turret, the responses of the structure in surge, heave, pitch and yaw are compared for all possible vertical locations of the turret. A mooring layout is desirable when it results in fewer natural periods for $T < 25$ s with smaller magnitude of the RAO peaks. For a given horizontal position, the turret depth corresponding to the best response is identified. Next, the process is repeated for all possible horizontal positions,

Fig. 6 Surge, heave, pitch and yaw RAOs of the wind-tracing FOWT to combined wind and wave loads for four depths of the turret at location B. Figure in color online

A, B, C and D, and the preferred layout of the mooring system is found by assessing the responses.

The RAOs of the structure to combined wind and wave loads at points A, B, C and D for four depths are presented in Figs. 5, 6, 7 and 8. In general, in all locations of the turret, some large peaks are observed over the wave periods. The magnitude of the peaks may not be practical due to the absence of structural damping effect. Moreover, RAOs in heave and yaw show a symmetric behavior as a function of the wave heading angle, β, and this is to be expected given that the aerodynamic load only contributes to the motions of the structure in surge and pitch.

In Fig. 5, the surge motions of the structure with turret at location A and four different depths, experience small peaks at approximately $T = 22$ s. The surge RAOs for the first three turret depths are almost similar and they decrease to smaller values for turret at 5 d under the SWL. Shown in Fig. 5, both heave and pitch RAOs undergo one and two

peaks, respectively, for approximately 21 s $\leq T \leq$ 23 s. However, the peaks in heave and pitch RAOs for turret at 5 d are considerably smaller than those at 2 d, 3 d and 4 d turret depths. Hence, among the four depths in Fig. 5 (at the horizontal point A), the RAOs of turret at 5 d depth are better.

The surge, heave, pitch and yaw RAOs of the wind-tracing FOWT with turret at location B and its four drafts are presented in Fig. 6. The surge motions of the structure do not undergo any peaks for $T \leq 25$ s compared to the first three turret depths. Similar to location A, peaks in heave and pitch RAOS are observed for approximately 21 s $\leq T \leq$ 23 s and the four depths of the turret. Furthermore, as the turret is located deeper under the platform, the peaks in heave and pitch become smaller. In conclusion, when the turret is located at horizontal location B, the depth 5 d results in better motions.

Shown in Fig. 7, the surge, heave, pitch and yaw motions of the wind-tracing FOWT does not change when the turret
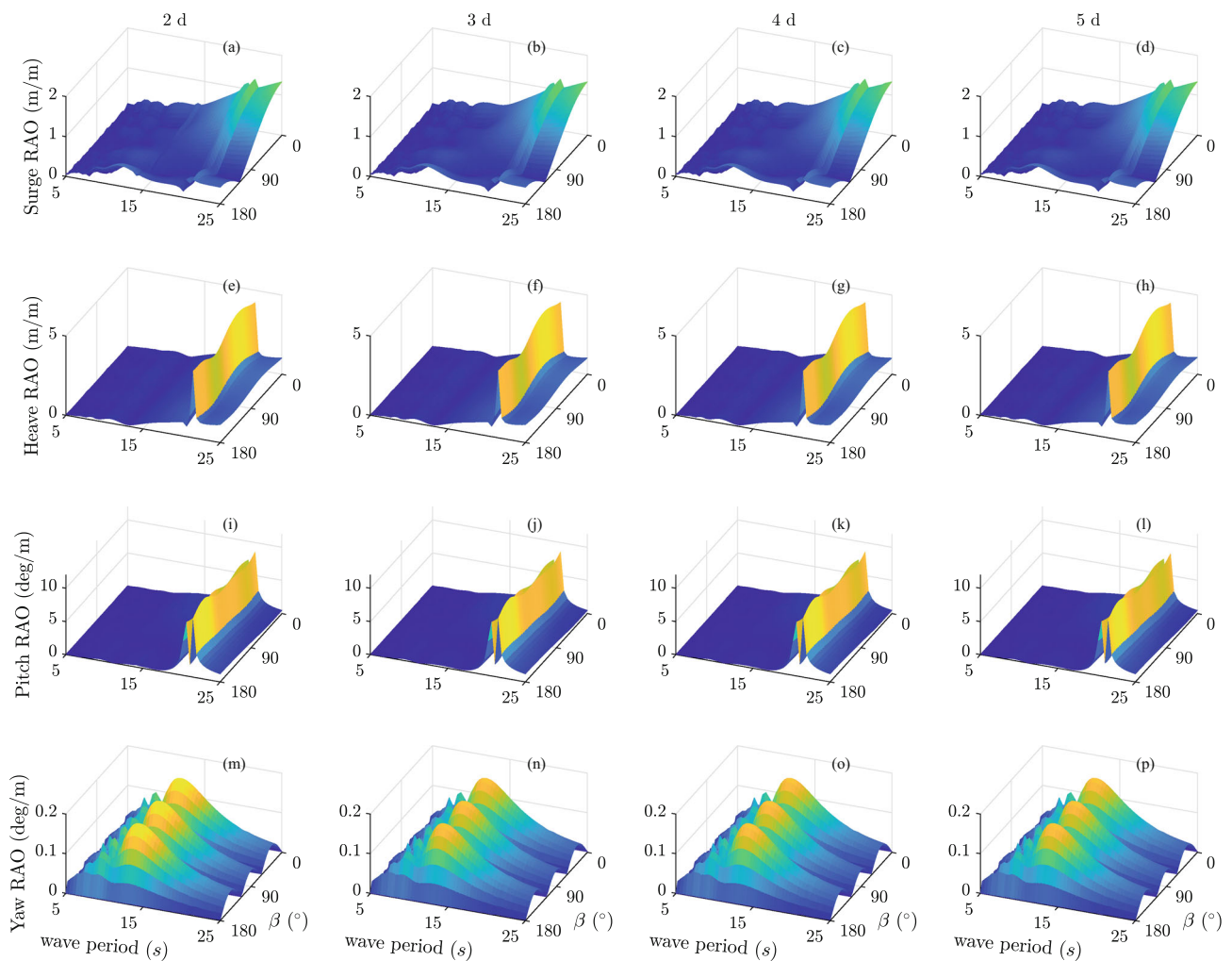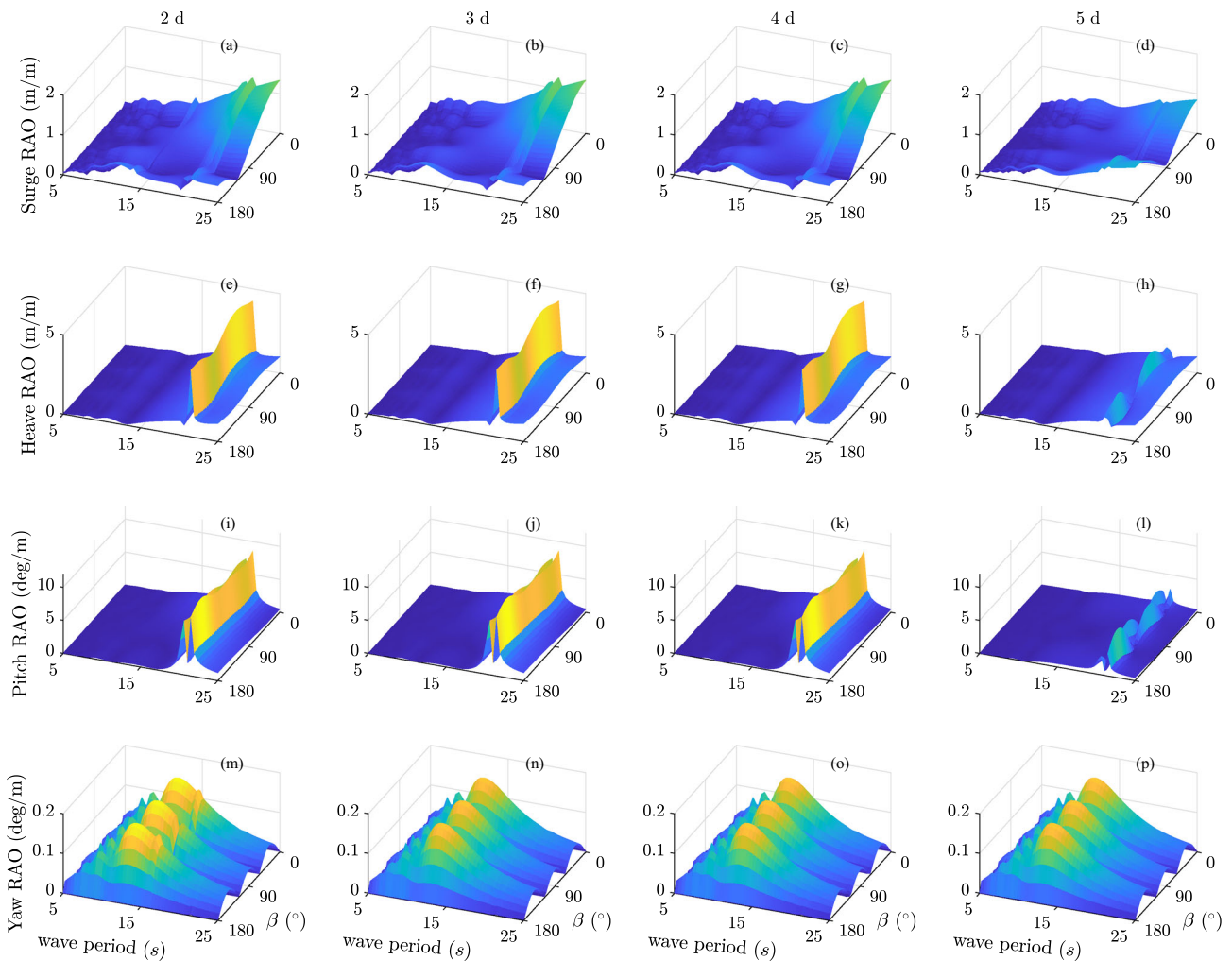
Fig. 7 Surge, heave, pitch and yaw RAOs of the wind-tracing FOWT to combined wind and wave loads for three depths of the turret at location C. Figure in color online

is located at point C and moves from $2\,d$ to $5\,d$ depth under the SWL. The structure undergoes large peaks in heave and pitch for wave periods smaller than 25 s. Although, the magnitude of the peaks are not realistic and practical, due to the resonances observed in heave and pitch RAOs, none of the turret depths at point C results in reasonable motions of the structure. Finally, presented in Fig. 8, the last four mooring configurations are with turret located at point D and specified four depths. Similar to the motions of the structure at location A, large peaks are observed in heave and pitch for $2\,d$, $3\,d$ and $4\,d$ turret depths and the largest turret depth, *i.e.* $5\,d$, results in smaller peaks and more desirable RAOs of the structure for $T \leq 25$ s.

In general, it can be seen that the middle two locations of the turret, locations B and C result in relatively larger peaks in heave and pitch motions of the structure. Moreover, it is observed that when the turret is at points A, B and D, as it

is located deeper under the platform the peaks are smaller. However, in our study, we assumed that the maximum depth of the turret is confined to $5\,d$ under the SWL. Finally, three locations of the turret out of the 16 configurations are chosen; point A with turret depth $5\,d$, point B with turret depth $5\,d$ and point D with turret depth $5\,d$. Comparing the RAOs in surge, heave and pitch for the chosen locations of the turret, the responses of the structure at point A with $5\,d$ below the SWL are determined to be best, since the peaks at this point in heave and pitch are smaller than other preferred configurations. Therefore, $x = 120.0$ m and $y = 0$ m is chosen as the optimum location of the turret based on the rigid-body motions of the structure to combined wind and wave loads. Thus, in the following subsections, the hydro- and aeroelastic analyses of the MUFOWT are carried out for this position of the turret.

Fig. 8 Surge, heave, pitch and yaw RAOs of the rigid wind-tracing FOWT to combined wind and wave loads for three depths of the turret at location D. Figure in color online

4.3 Rigid-body responses to wave loads

As discussed in previous sections, the turret located at point A and 5 d below the SWL results in optimum responses. The RAOs of the structure with the optimum location of the turret to combined wind and wave loads are shown in Fig. 6. Here, frequency dependent coefficients of the wind-tracing FOWT in its rigid-body modes and its RAOs to wave loads are presented and discussed.

The added mass and damping coefficients in surge, heave, pitch and the coupling component of surge and pitch are presented in Fig. 8. The added mass and damping coefficients depend on the geometry of the structure and experience some oscillations for wave frequencies $\omega < 2$ rad/s (wave period less than about 3 s). Moreover, the nonzero off-diagonal components imply the absence of the body symmetry with respect to the y-axis.

Translational and rotational responses of the wind-tracing FOWT are shown and compared in Fig. 10 for three wave heading angles, $\beta = 0°$, $\beta = 15°$ and $\beta = 30°$. Shown in Fig. 10, other than sway and yaw, the RAOs of the structure undergo small changes in their magnitude as the wave heading angle increases. However, as expected, increasing β results in larger sway and yaw motions of the wind-tracing FOWT. Furthermore, the natural periods of the rigid structure in heave, roll and pitch are 27.78 s, 21.42 s and 20.44 s, respectively. Peaks at these three natural periods are observed in the motions of the structure in heave, roll and pitch, see Fig. 10.

4.4 Elastic responses to wave loads

The optimum layout of the mooring system is identified considering the rigid-body motions of the structure. However, with the large characteristic length of the platform, the elas-

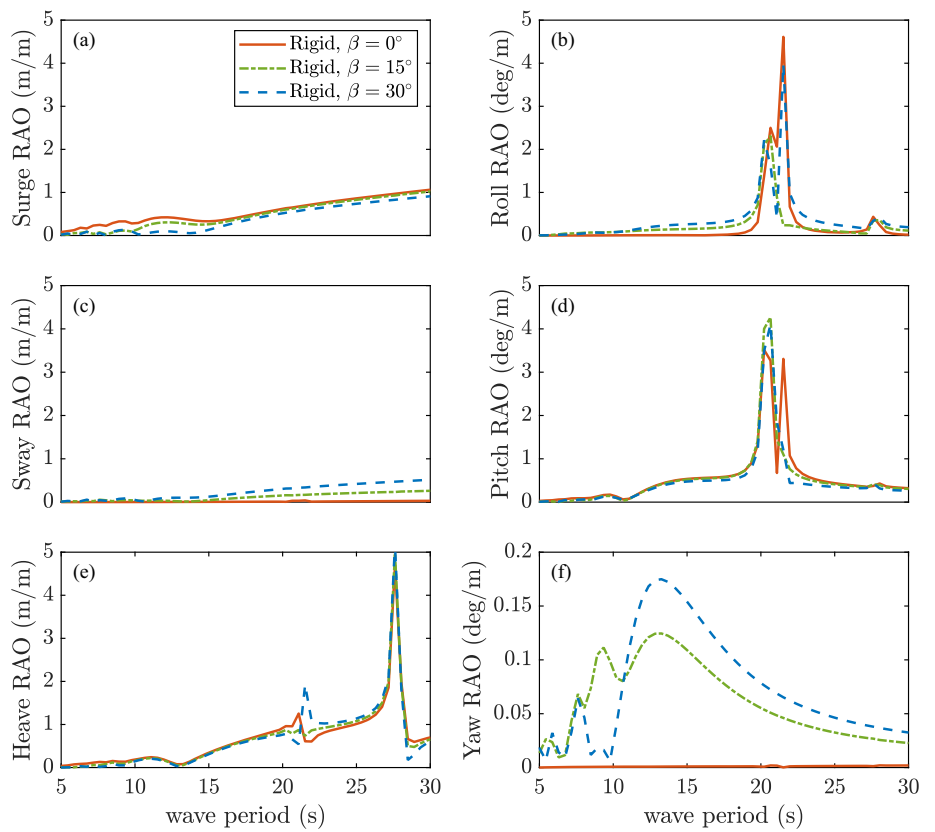**Fig. 9** Added mass and damping coefficients of the wind-tracing FOWT in surge, pitch and heave degrees of freedom
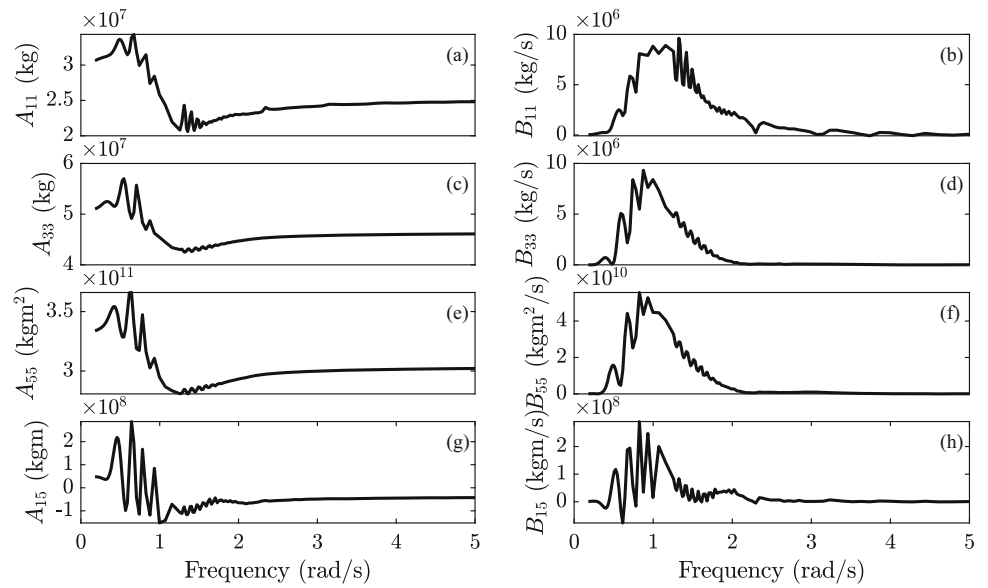
Fig. 10 RAOs of the rigid wind-tracing FOWT to wave loads with heading angles $\beta = 0°$, $\beta = 15°$ and $\beta = 30°$

ticity effect of the substructure and its coupling with the three wind turbines can affect its motions to combined wind and wave loads. In this subsection, the flexibility of the substructure together with the wind turbines are considered. The frequency-dependent hydrodynamic coefficients of the wind-tracing FOWT and its wet natural frequencies are presented. Next, the motions of the flexible wind-tracing FOWT to wave loads are obtained and compared with its rigid-body motions

The eigenvalue analysis of the complete structure is performed for its first 13 dry modes. That is, hydrodynamic analysis of the structure is carried out for its six translational and rotational rigid-body and the added 7 generalized modes for elasticity. The first four wet natural periods of the structure connected to the turret-bearing system are presented in Fig. 11. It can be seen that the mode-shapes of the structure are dominated first by the flapwise and edgewise deflections

Fig. 11 The **a** 7th, **b** 8th, **c** 9th and **d** 10th wet natural mode-shapes of the wind-tracing FOWT connected to the turret bearing system (The displacements are magnified by a factor of 5000)

(a)

(b)

(c)

(d)
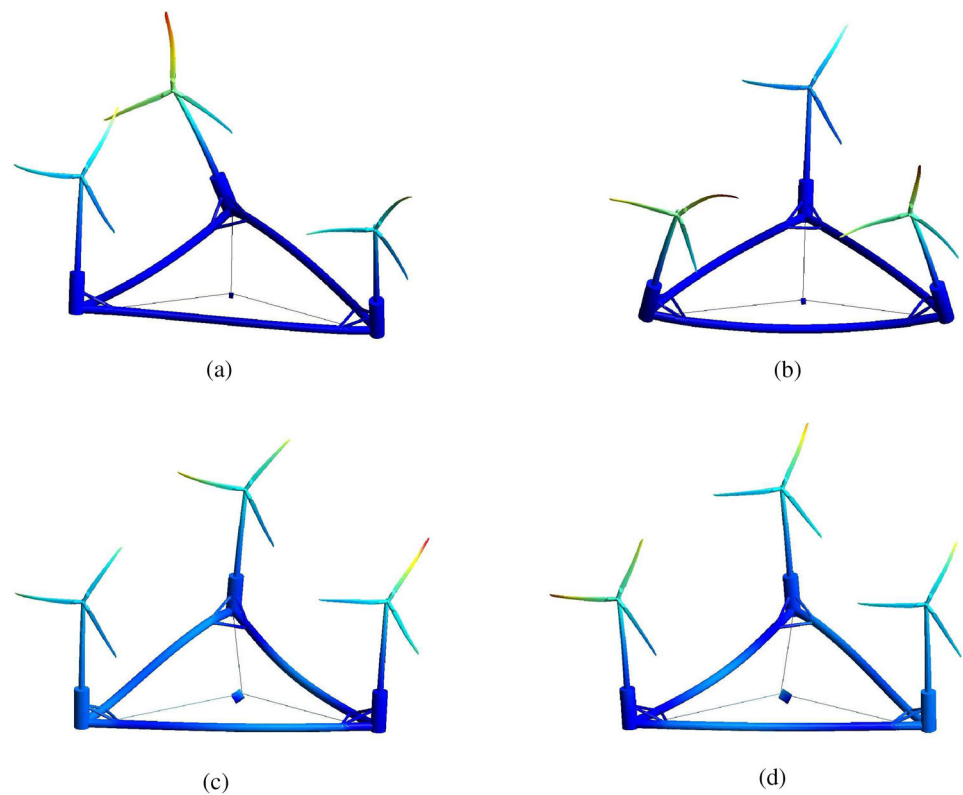
Fig. 12 The normalized added mass and damping coefficients of the wind-tracing FOWT for its first four generalized modes
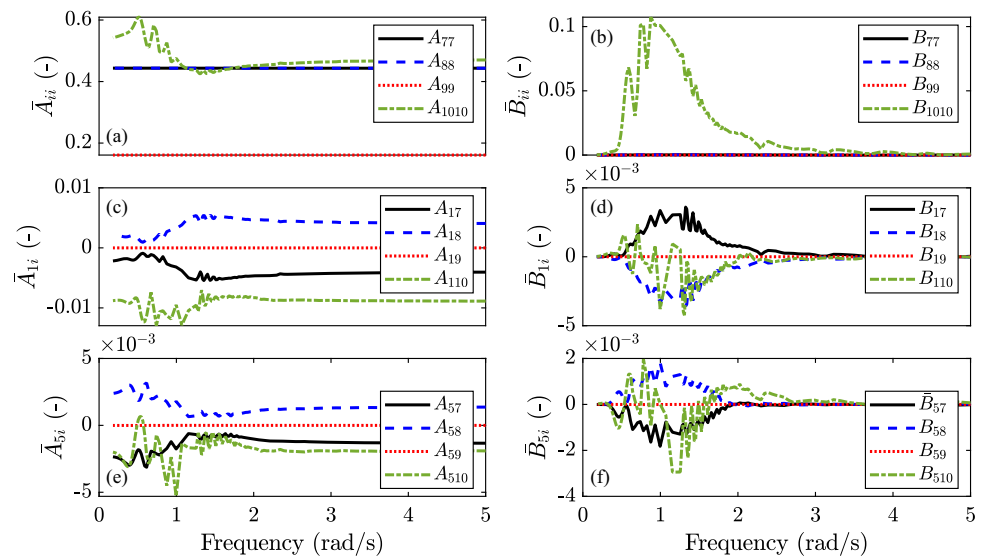
of the blades and second by the side-side deflections along the towers. The deflections of the pontoons are very small for the first two wet mode-shapes of the structure.

The mass normalized added mass and hydrodynamic damping coefficients for the first four generalized modes and their couplings with surge and pitch are shown in Fig. 12. For comparison, the coupling components of the generalized modes with surge and pitch are normalized with the mass of the structure and the pitch rotational inertia, respectively.

The frequency-dependent coefficients for both the rigid-body and generalized modes are computed with some oscillations at wave frequencies smaller than 2 rad/s; see Figs. 9 and 12, respectively. The magnitude of the frequency-dependent coefficients at the generalized modes are significantly larger than their coupling coefficients with the rigid-body modes; see Fig. 9. Shown in Fig. 12, for $\omega > 1$ rad/s, the normalized diagonal added mass coefficients have approximately similar magnitudes for the first four generalized modes. Among
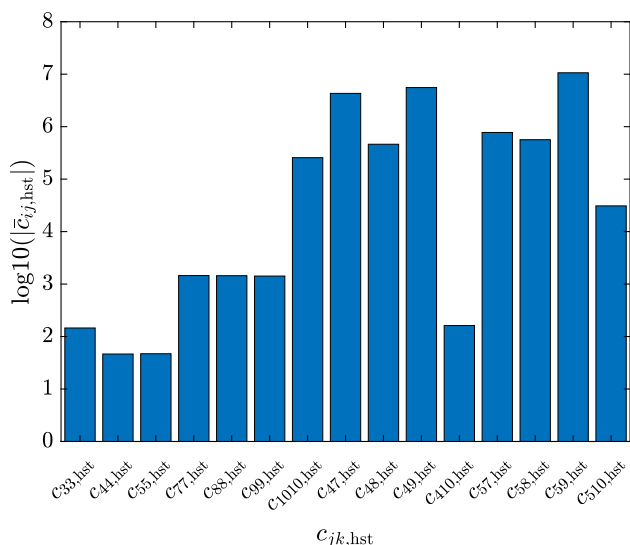
Fig. 13 Normalized hydrostatic restoring coefficients of the flexible wind-tracing FOWT for heave, roll and pitch and the first four generalized modes
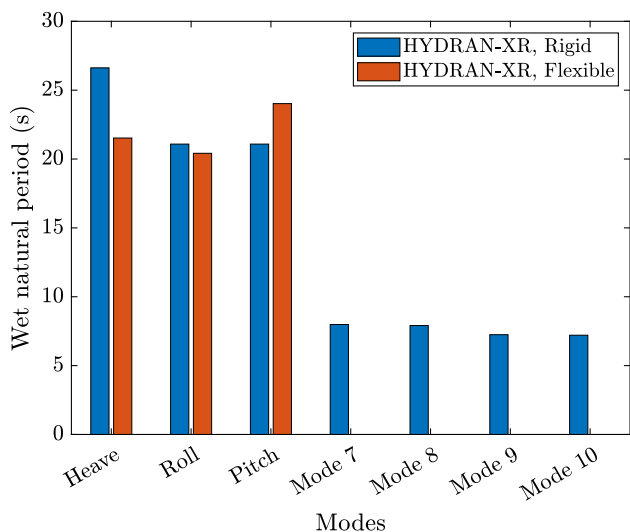

Fig. 14 Comparison of the wet natural frequencies of the rigid and flexible wind-tracing FOWTs in heave, roll and pitch and the computed first four generalized wet natural frequencies
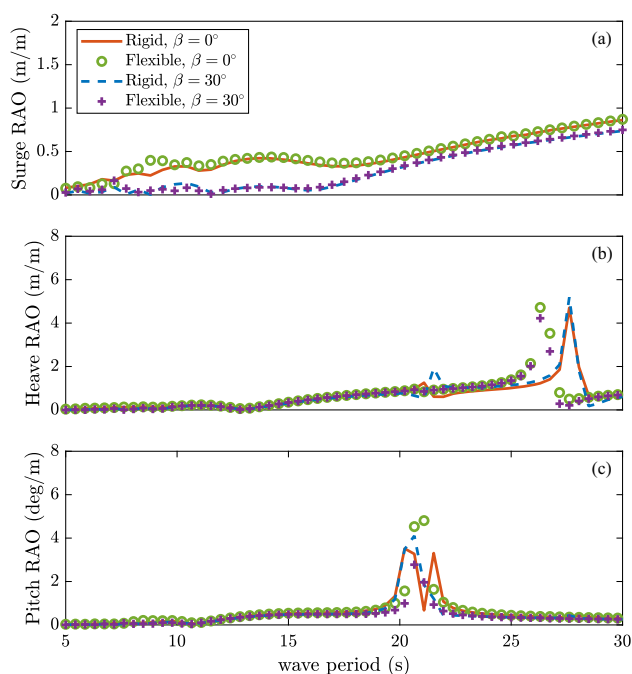

Fig. 15 Comparison of the wave-induced RAOs of fully flexible and rigid wind-tracing FOWT for two wave heading angles, $\beta = 0°$ and $30°$

the added mass coupling components with surge, A_{19} and A_{18} have the least and the largest contributions, respectively. Similar behavior in added mass coefficients of coupling generalized modes with pitch is observed. Furthermore, the hydrodynamic damping coefficients for modes 7, 8 and 9 are approximately zero resulting in largest contributions to the normalized diagonal coefficients at mode 10. Finally, among the coupling modes of the normalized hydrodynamic damping coefficients with surge and pitch, B_{19} and B_{59} have the smallest magnitude.

Figure 13 presents the normalized hydrostatic restoring coefficients of the flexible wind-tracing FOWT for heave, roll

and pitch and its first 4 generalized modes. Only the nonzero coefficients for the coupling modes of roll and pitch with the generalized modes are presented. To compare the magnitude of the restoring coefficients, they are normalized by the roll and pitch rotational inertia, respectively. Shown in Fig. 13, the magnitude of the normalized restoring coefficients for the first two generalized modes, 6 and 7, are considerably larger than other hydrostatic coefficients. Furthermore, among the coupling modes of the generalized modes and roll and pitch degrees of freedom, c_{410} shows the largest magnitude.

The wet natural frequencies of the flexible wind-tracing FOWT for $T \leq 35$ s are computed by HYDRAN-XR and presented in Fig. 14. Three of the wet natural periods of the structure in its rigid-body modes namely; heave, roll and pitch are within the considered interval of the wave periods and are compared with those of the rigid wind-tracing FOWT. When elasticity of the structure is considered, the natural periods of the structure in heave and roll decrease to smaller values. Shown in Fig. 14, the first four wet generalized natural periods occur in smaller wave periods and are approximately 7 s $< T < 8$ s. The wet natural frequencies for the first four generalized modes are within the wave periods considered for the aero- and hydroelasticity of the wind-tracing FOWT. Hence, some resonances due to the generalized modes 7, 8, 9 and 10 may be seen in the RAOs.

The responses of the flexible structure can be different from its rigid-body counterparts due to the coupling effects of the generalized and the rigid-body modes. In the following,

Fig. 16 The total **a** wave-induced horizontal shear force and **b** overturning moment about *y*-axis at the SWL on column 1, the total **c** wave-induced horizontal shear force and **d** overturning moment about *y*-axis at the SWL on column 2, and the total **e** wave-induced horizontal shear force and **f** overturning moment about *y*-axis at the SWL on column 3 for three incident wave heading angles, $\beta = 0°$, 30° and 60°
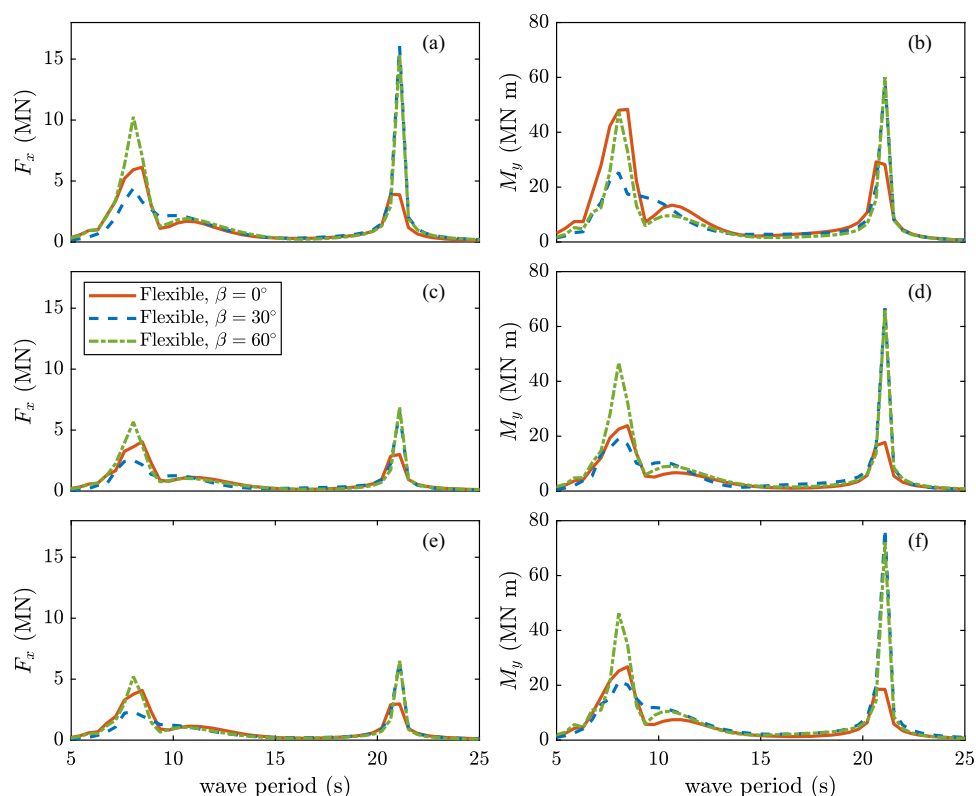
the elasticity effects of the wind-tracing FOWT in its wave-induced motions are shown and discussed.

The RAOs of the wind-tracing FOWT to incoming wave loads are presented in Fig. 15 for both rigid- and flexible-body cases and wave heading angles $\beta = 0°$ and $\beta = 30°$. In general, the magnitude of the peaks are not realistic and practical, due to lack of structural damping. Furthermore, the magnitude of surge and pitch RAOs are slightly decreased when the wave heading angle is changed to $\beta = 30°$. As shown earlier in Fig. 14, the heave natural frequencies of the rigid and flexible structures are approximately 27.6 s and 26.8 s, respectively ($\omega \approx 0.23$ rad/s), which are observed in heave RAOs by the rigid and flexible bodies. The pitch RAOs of the flexible structure experience a peak at approximately 21.1 s, the natural period of roll and pitch when elasticity is considered. Similarly, the rigid-body pitch RAOs undergo two peaks at approximately 21.42 s and 20.44 s, the natural periods of roll and pitch of the rigid structure. Moreover, due to the natural periods of the first four generalized modes at approximately 7 s to 8 s, some peaks are observed in surge by the flexible FOWT.

Figure 16 presents the wave-induced total horizontal shear force, F_x and the total overturning moment about *y*-axis, on cross-sections of columns 1, 2 and 3 at the SWL. The shear forces and overturning moments are presented for three incident wave heading angles $\beta = 0°$, 30° and 60° and for wave periods $5 \text{ s} \leq T \leq 35 \text{ s}$. Commonly, two large peaks at

approximately $T = 8$ s and $T = 20.44$ s, the wet natural frequencies of the fourth generalized mode and pitch of the wind-tracing FOWT, are observed in F_x and M_y for the three columns and in three wave heading angles. Moreover, column 1 experiences the largest peaks at these wave periods in comparison with other two front columns. The total shear force and the overturning moments computed for columns 1 and 2 are approximately comparable.

The wave-induced horizontal nodal displacements along the towers of the flexible wind-tracing FOWT are presented in Fig. 14 for wave periods 10 s, 15 s and 20 s and $\beta = 0°$ and 90° and are compared with its rigid-body counterparts. The horizontal displacements of the rigid towers are due to the combined effect of surge and pitch motions of the structure. The displacements of the flexible structure in its generalized modes in addition to its surge and pitch motions contribute to the horizontal displacements along its towers.

Shown in Fig. 17, the nodal displacements are presented for wave periods 10 s, approximately close to its four generalized wet natural periods, 15 s and 20 s, slightly smaller than the roll and pitch natural periods of the rigid and flexible wind-tracing FOWTs. The horizontal displacements are computed for 54 nodes along the tower from its base, $z = 22$ m, upto its tip, $z = 109$ m. For this analysis, the nodes at the leading edges of the towers, facing the incoming wind are identified. In Fig. 17, the horizontal displacements are presented separately for the rear tower, tower 1, at the front

Fig. 17 Comparison of the horizontal wave-induced nodal displacements of towers 1, 2 and 3 for the rigid and fully flexible wind-tracing FOWT with $\beta = 0°$ and 90° and wave periods 10 s, 15 s and 20 s
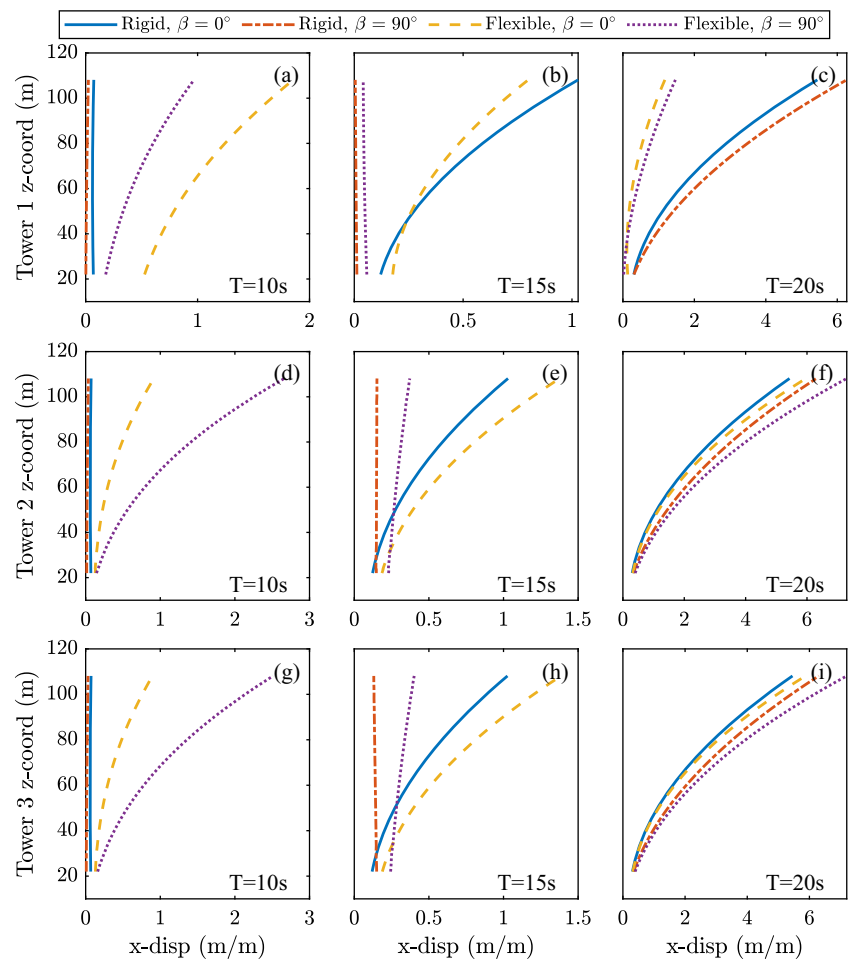

left corner of the wind-tracing platform, tower 2 and at the front right corner of the wind-tracing platform, tower 3; see Fig. 1b. In general, the horizontal displacements of towers 2 and 3 are almost comparable for the considered wave periods and with $\beta = 0°$ and are slightly larger than those by tower 1. Comparing the nodal displacements for the three different wave periods and two wave heading angles, the largest nodal displacements are observed at $T = 20$ s by the rigid tower 1 and flexible towers 2 and 3. Furthermore, at $T = 10$ s, the flexible towers undergo considerably larger nodal displacements in both wave heading angles compared with the rigid towers. At $T = 15$ s, the horizontal nodal displacements by both rigid and flexible structures with $\beta = 90°$ are the smallest compared with those computed for rigid and flexible structures in head seas.

Next, the vertical nodal displacements of the three pontoons at the vertical plane, xz-plane, are presented in Fig. 18. The nodal displacements are given for each pontoon of the triangular platform, pontoon 1, pontoon 2 and pontoon 3, see Fig. 1a. The z-displacements of the flexible pontoons are

due to heave and roll, and their coupling effect with the generalized modes. The displacements computed for the rigid pontoons lack the contribution of the generalized modes.

In Fig. 18, the vertical displacements along the pontoons are presented for three wave periods, $T = 10$ s, $T = 15$ s and $T = 20$ s and two wave heading angles, $\beta = 0°$ and 90°. The nodal displacements are computed for 104 nodes along the pontoons, at their outer edge, facing outside the triangle with draft -12 m. Shown in Fig. 18, the nodal displacements of the pontoons are reported over their length, where the length of pontoons 1 and 2 are measured with respect to column 1 and the length of pontoon 3 is given with respect to column 2. Hence, both pontoons 1 and 2 show comparable displacements in z-direction for $\beta = 0°$ and three wave periods. However, by increasing the wave heading angle to $\beta = 90°$, the z-displacements of pontoon 1 is larger than pontoon 2 for the three wave periods. Considering pontoon 3, the vertical nodal displacements show almost a bell curve for the wave periods and heading angles considered here, reaching to its largest magnitude at $T = 20$ s in head seas.

Fig. 18 Comparison of the wave-induced vertical nodal displacements of pontoons 1, 2 and 3 for the rigid and fully flexible wind-tracing FOWT with $\beta = 0°$ and 90° and wave periods 10 s, 15 s and 20 s
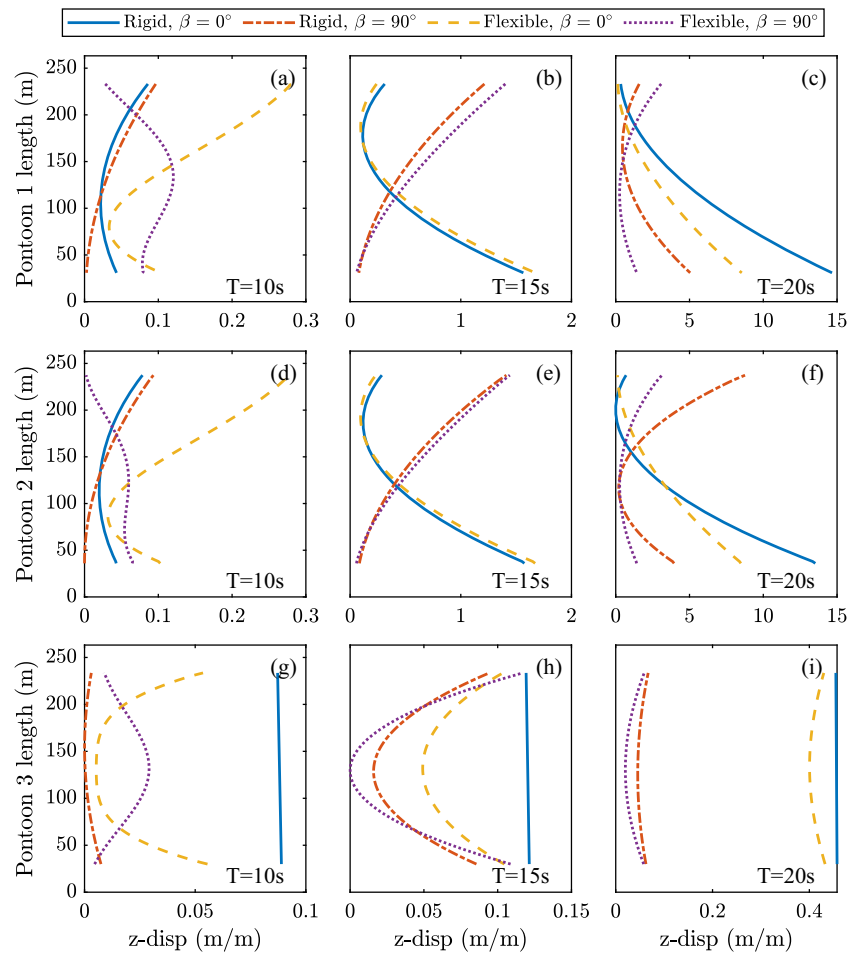
4.5 Elastic responses to combined wind and wave loads

In this section, the aero- and hydroelastic responses of the fully flexible wind-tracing FOWT to combined wind and wave loads are presented. The RAOs of the flexible structure due to regular waves and steady wind are computed and compared with its rigid-body counterpart. Following the discussion of the previous section, the total horizontal shear force and overturning moment about y-axis, the nodal displacements along the towers and the pontoons are presented.

Surge, heave and pitch RAOs of the wind-tracing FOWT to combined wind and wave loads are shown in Fig. 19 for two wave heading angles 0° and 30° and for both rigid- and flexible-body cases.

Shown in Fig. 16, the surge and pitch motions of the rigid structure to combined waves and wind loads are larger than those by the flexible wind-tracing FOWT with both wave heading angles. The peaks in both heave and pitch RAOs at the natural periods of the rigid and flexible structures are in larger magnitude when the wind loads are present. Moreover, due to the coupling between surge and pitch, the surge
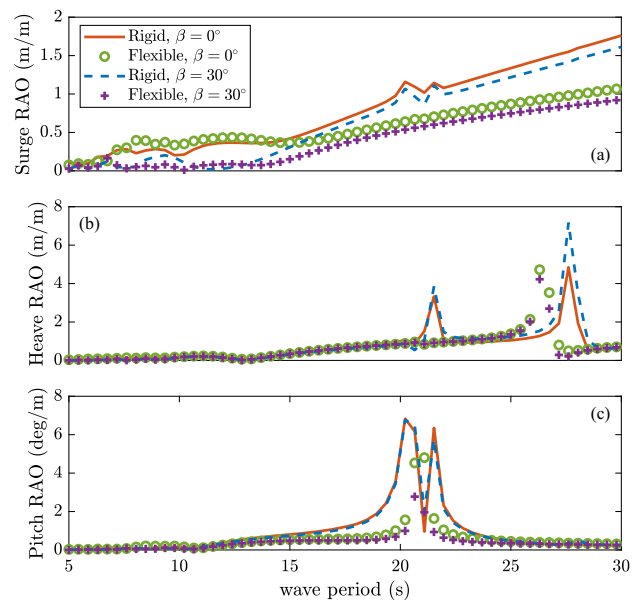

Fig. 19 Comparison of the combined wind- and wave-induced RAOs of fully flexible and rigid wind-tracing FOWT for two wave heading angles, $\beta = 0°$ and 30°

Fig. 20 The total **a** Horizontal shear force and **b** Overturning moment about y-axis at the SWL on column 1, the total **c** Horizontal shear force and **d** Overturning moment about y-axis at the SWL on column 2, and the total **e** Horizontal shear force and **f** Overturning moment about y-axis at the SWL on column 3 to combined wave and wind loads for three incident wave heading angles, $\beta = 0^{acirc}$, 30° and 60°
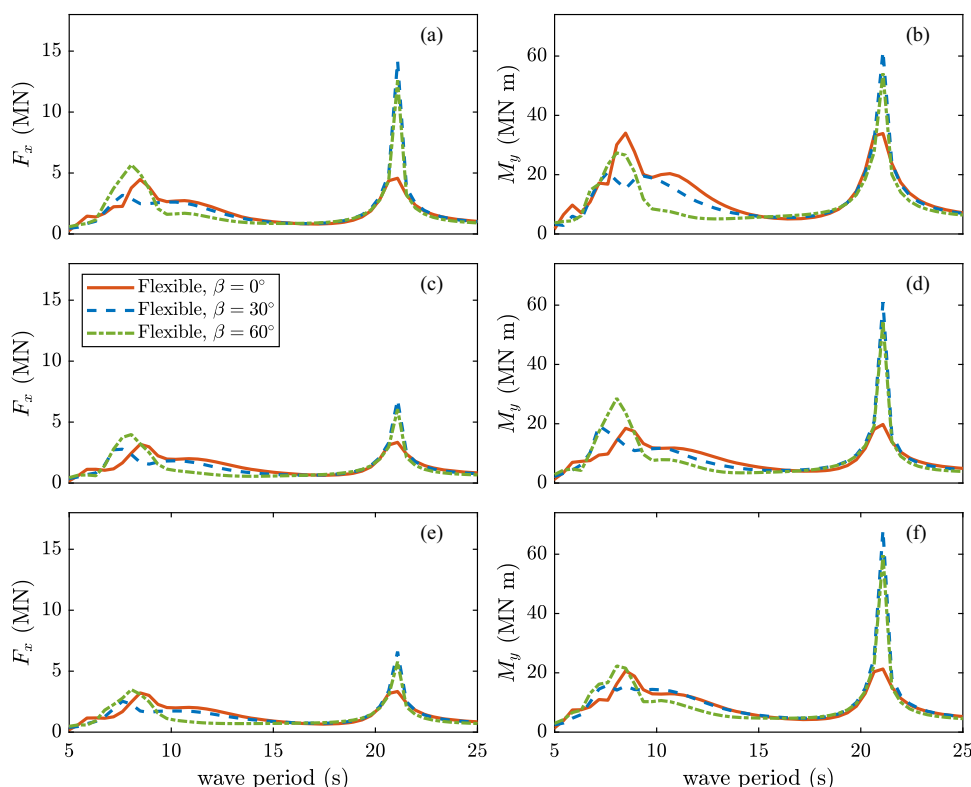

motions of the flexible structure show a peak at approximately $T = 21.1$ s, the pitch natural period of the flexible wind-tracing FOWT. Since the incoming wind is orthogonal to the rotors, only the surge and pitch motions of the structure will be influenced by the addition of the aerodynamic loads. Hence, the heave RAOs of both rigid and flexible bodies are approximately comparable to those presented in Fig. 15 in the absence of the wind loads.

Similar to the previous section, the total horizontal shear forces and overturning moments about the y-axis to combined waves and wind at cross-sections of the three columns, on the SWL are shown in Fig. 20. Comparing the presented F_x and M_y for the three columns in Fig. 20 to their counterparts in Fig. 16, it can be seen that with the addition of wind loads, the magnitude of the peaks at $T = 8$ s and $T = 21.1$ s become smaller. Furthermore, the overturning moments on the three

columns are larger for approximately $8 \text{ s} \le T \le 15$ s when the aerodynamic loads are added.

The nodal displacements of the towers and the pontoons under combined wind and wave loads are calculated and presented in Figs. 21 and 22, respectively. With the addition of the wind load, the nodal displacements of the towers and pontoons are decreased significantly for both rigid- and flexible-body cases compared with those when the wind load was absent. Generally, at the three wave periods and the two wave heading angles, the top of the towers undergo the largest horizontal displacements. Moreover, tower 1 experiences the largest difference in its nodal displacements when the wave heading angle changes from head seas to $\beta = 90°$. In addition, the front towers experience larger nodal displacements compared with tower 1 on the rear column of the wind-tracing platform.

Fig. 21 Comparison of the horizontal nodal displacements of towers 1, 2 and 3 for the rigid and fully flexible wind-tracing FOWT to combined wind and wave loads with $\beta = 0°$ and 90° and wave periods 10 s, 15 s and 20 s
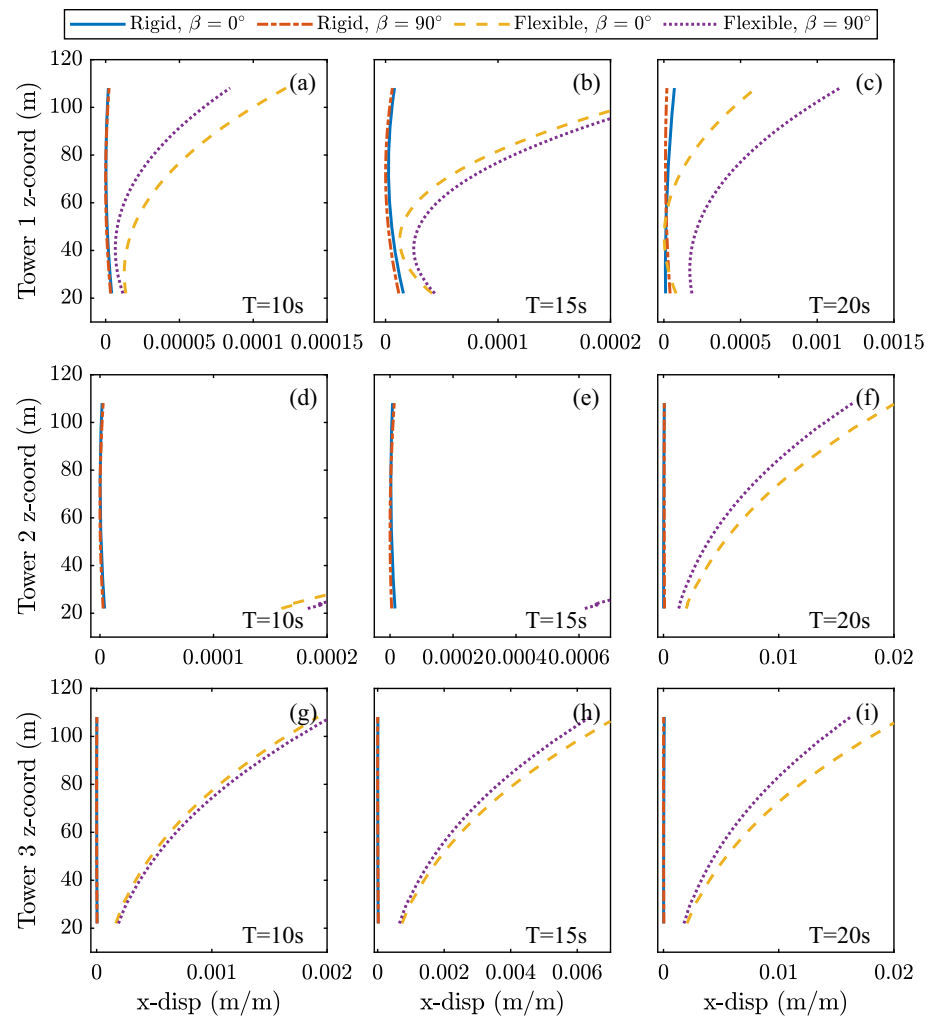
Similar to the previous section, under combined wind and wave loads, the nodal vertical displacements of pontoons 1, 2 and 3 are computed for two wave heading angles, 0° and 90° and three wave periods 10 s, 15 s and 20 s. Figure 22, presents and compares the nodal displacements for rigid and flexible pontoons under combined wind and wave loads. Compared with Fig. 18, the addition of the wind load, results in smaller displacements along the three pontoons at the three wave periods. Pontoons 1, 2 experience their largest displacements

when flexible with $\beta = 90°$ at $T = 20$ s. However, pontoon 3 undergoes a bell-shape vertical deflection when flexible and experiences its largest displacements at the middle of the pontoon at $T = 20$ s with head seas waves. By changing the wave heading angle, the wave loads on pontoons 2 and 3 are not symmetric, which results in different nodal displacements in z-direction. This can be seen in Fig. 22d–i for the computed displacements.

Fig. 22 Comparison of the vertical nodal displacements of pontoons 1, 2 and 3 for the rigid and fully flexible wind-tracing FOWT to combined wind and wave loads with $\beta = 0°$ and $90°$ and wave periods 10 s, 15 s and 20 s
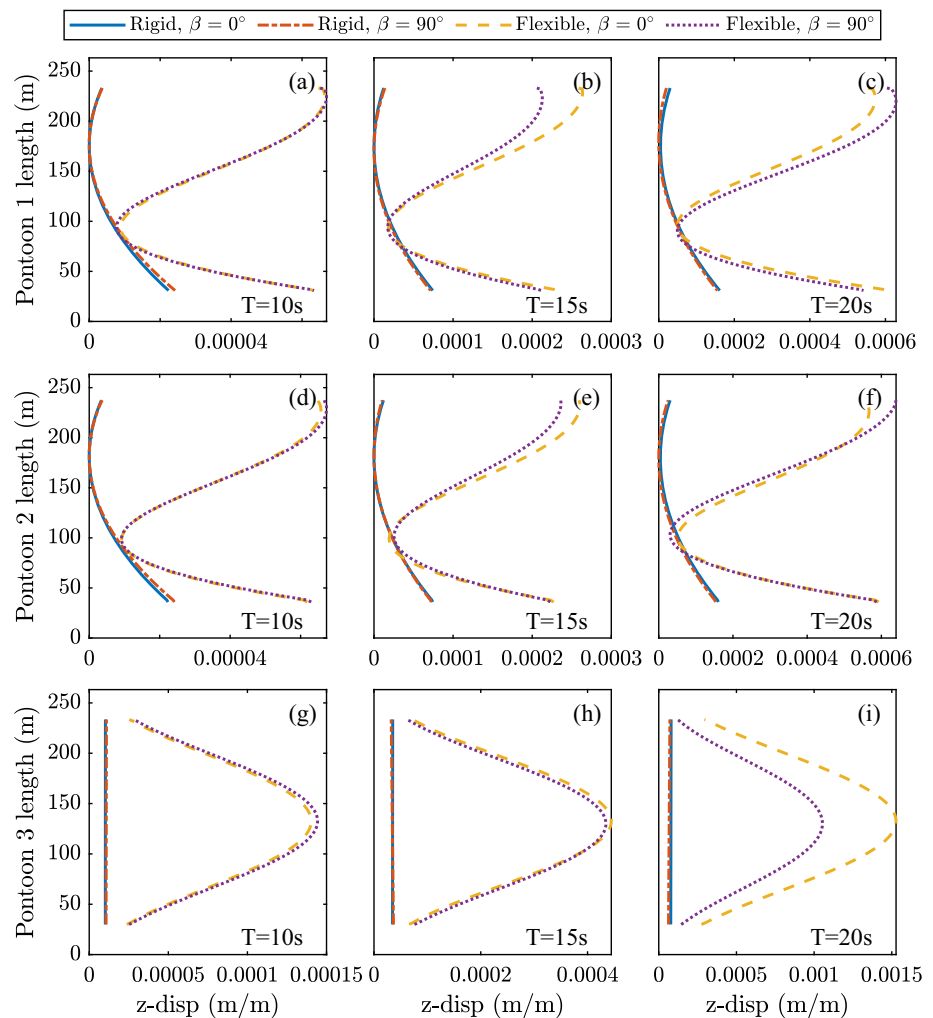
5 Concluding remarks

In this study, the dynamic motions and elastic responses of a MUFOWT to waves and combined wind and wave loads are analyzed and reported. The aero- and hydroelasticity analyses of the MUFOWT is conducted by a numerical coupling approach namely an enhanced version of HYDRAN-XR. HYDRAN-XR is able to account for multiple towers supported by a single platform and consists of three sections on hydrodynamic, aerodynamic and finite-element method analyses.

In our numerical approach, the governing equations of motion are solved in frequency domain. The hydrodynamic and aerodynamic analyses are based on linear wave diffraction theory and steady BEM method, respectively. In HYDRAN-XR, the aerodynamic load is distributed as nodal forces along the front face of the blades and the towers. If elasticity of the FOWT is of interest, the dry modes of the structure are computed with the finite-element module. The computed natural dry modes are added as generalized modes

to the governing equations of motions for both hydrodynamic and aerodynamic analyses.

The wind-tracing FOWT considered in this study is a triangular platform that supports three 5 MW NREL wind turbines and is moored to the seabed with a turret-bearing mooring system. The turret-bearing mooring system allows the structure to align itself to the direction of the dominant environmental loads and reduces the yaw moment on the turret. An optimization is conducted to study the self-alignment mechanism of the structure and identify the preferred location of the turret for its mooring system. The motions of the rigid wind-tracing FOWT to combined wave and wind loads are computed for four horizontal locations of the turret with four different depths under the substructure. The RAOs of the structure in surge, heave, pitch and yaw are compared for the 16 different locations of the turret with co-directional and misaligned wind and wave loads, and a preferred configuration of the mooring system is found.

Finally, with the identified turret location, the fully flexible wind-tracing FOWT is modeled and its motions to wave loads

and combined wind and wave loads are determined. With aero- and hydroelasticity analyses, the RAOs of the flexible structure, horizontal shear forces and overturning moments on the columns and distribution of nodal displacements along its pontoons and the towers are obtained and presented.

In the present study, the significance of the weathervaning mechanism of the wind-tracing FOWT on its responses is investigated. It is shown that by changing the layout of the mooring system, the motions of the structure to combined wind and wave loads can change significantly. Furthermore, comparison of the rigid- and flexible body motions of the wind-tracing FOWT indicates that elastic motions of the wind-tracing FOWT are not negligible and should be considered. In addition, the effect of the flexibility of the wind-tracing FOWT on its motions can be significant for misaligned wind and wave loadings.

MUFOWTs are at the concept stage, which require specific attention due to their complex configurations and characteristics. Both rigid-body responses and elastic deformations of the tower and the floating body should be considered. The presented study shows that HYDRAN-XR can be a powerful and useful numerical tool for elasticity and motion analysis of MUFOWT in co-directional and misaligned wind and wave loading conditions.

References

Bae YH, Kim MH (2014) Coupled dynamic analysis of multiple wind turbines on a large single floater. Ocean Eng 92:175–187. https://doi.org/10.1016/j.oceaneng.2014.10.001

Bae YH, Kim MH (2015) The dynamic coupling effects of a MUFOWT (multiple unit floating offshore wind turbine) with partially broken blade. J Ocean Wind Energy 2:89–97

Barltrop N (1993) Multiple unit floating offshore wind farm (MUFOW). Wind Eng 17:183–188

Bashetty S, Ozcelik S (2020) Design and stability analysis of an offshore floating multi-turbine platform. In: 2020 IEEE green technolo-

gies conference (GreenTech), April 1–3, Oklahoma, United States, pp 1–6

Bashetty S, Ozcelik S (2020a) Aero-hydrodynamic analysis of an offshore floating multi-wind-turbine platform—part I. In: 2020 IEEE 3rd international conference on renewable energy and power engineering (REPE), IEEE, October 9–11, Edmonton, Canada, pp 1–6

Bashetty S, Ozcelik S (2020b) Aero-hydrodynamic analysis of an offshore floating multi-wind-turbine platform—part II. In: 2020 IEEE 3rd international conference on renewable energy and power, October 9–11, Edmonton, Canada, pp 1–6

DNV (Det Norske Veritas) (2015) DNV-GL-OS-E302 Offshore Mooring Chain. Technical Report 2013. DNV

Farr H, Ruttenberg B, Walter RK, Wang YH, White C (2021) Potential environmental effects of deepwater floating offshore wind energy facilities. Ocean Coast Manag 207:1–16. https://doi.org/10.1016/j.ocecoaman.2021.105611

Global Maritime Moorlink (2016) Product Catalogue 2016. Technical Report, Global Maritime Moorlink

Hanssen JE, Margheritini L, O'Sullivan K, Mayorga P, Martinez I, Arriaga A, Agos I, Steynor J, Ingram D, Hezari R, Todalshaug JH (2015) Design and performance validation of a hybrid offshore renewable energy platform. In: 2015 tenth international conference on ecological vehicles and renewable energies (EVER), IEEE, March 31–April 2, Monte-Carlo, Monaco, pp 1–8. https://doi.org/10.1109/EVER.2015.7113017

Henderson AH, Patel MH (2000) Floating offshore wind farms—an option? In: Offshore wind energy in Mediterranean and Other European Seas, April 13–15, Siracusa, Sicilia, Italy, pp 1–15

Henderson AH, Patel MH (2003) On the modelling of a floating offshore wind turbine. Wind Energy 6:53–86. https://doi.org/10.1002/we.83

Hu C, Sueyoshi M, Liu C, Liu Y (2014) Hydrodynamic analysis of a semi-submersible-type floating wind turbine. J Ocean Wind Energy 1:202–208

Huang LL, Riggs HR (2000) The hydrostatic stiffness of flexible floating structures for linear hydroelasticity. Mar Struct 13:91–106

Huang AS, Moreno FM, Tannuri EA, Câmara JGA (2019) Equilibrium position analysis for offloading operations with turret-moored FPSO. J Offshore Mech Arct Eng 141:1–9. https://doi.org/10.1115/1.4042531

Ishihara T, Van Phuc P, Sukegawa H (2007a) A numerical study on the dynamic response of a floating offshore wind turbine system due to resonance and nonlinear wave. In: 2nd European offshore wind (EOW) conference, December 4–6, Berlin, Germany, pp 4–6

Ishihara T, Van Phuc P, Sukegawa H, Shimada K, Ohyama T (2007b) A study on the dynamic response of a semi-submersible floating offshore wind turbine system. Part 1: a water tank test. In: 12th international conference on wind engineering, July 1–6. Cairns, Australia, pp 2511–2518

Jang HK, Kim HC, Kim MH, Kim KH (2015) Coupled dynamic analysis for multi-unit floating offshore wind turbine in maximum operational and survival conditions. In: ASME 34th international conference on ocean, offshore and Arctic engineering, OMAE2015, ASME, May 31–June 5, Newfoundland, pp 1–8. https://doi.org/10.1115/OMAE2015-42062

Jonkman JM, Butterfield S, Musial W, Scott G (2009) Definition of a 5-MW reference wind turbine for offshore system development. Technical Report, National Renewable Energy Laboratory (NREL), Golden, CO

Jonkman JM, Wright AD, Hayman GJ, Robertson AN (2018) Full-system linearization for floating offshore wind turbines in OpenFAST. In: 1st international offshore wind technical conference, November 4–7, San Francisco, CA, USA, pp 1–10. https://doi.org/10.1115/iowtc2018-1025

Kang HY, Kim MH, Kim KH, Hong KY (2017) Hydroelastic analysis of multi-unit floating offshore wind turbine platform (MUFOWT).

In: Proceedings of the international offshore and polar engineering conference, June 25–30, San Francisco, CA, pp 554–560

Kim MH, Ran Z, Zheng W (2001) Hull/mooring coupled dynamic analysis of a truss spar in time-domain. Int J Offshore Polar Eng 11:301–308

Kvittem MI, Moan T (2014) Frequency versus time domain fatigue analysis of a semisubmersible wind turbine tower. J Offshore Mech Arct Eng 137:1–11. https://doi.org/10.1115/1.4028340

Lamei A, Hayatdavoodi M (2020) On motion analysis and elastic response of floating offshore wind turbines. J Ocean Eng Mar Energy 6:71–90. https://doi.org/10.1007/s40722-019-00159-2

Lamei A, Hayatdavoodi M, Riggs HR (2022) Motion and elastic deformations of floating offshore wind turbines due to combined wind and waves. J Renew Sustain Energy **(submitted and under review)**

Lamei A, Hayatdavoodi M, Wong C, Tang B (2019) On motion and hydroelastic snalysis of a floating offshore wind turbine. In: ASME 2019 38th international conference of ocean, offshore and arctic engineering, OMAE 2019, ASME, June 9–14. Glasgow, UK, pp 1–10

Lee J, Zhao F (2022) Global offshore wind report 2022. Technical Report, Global Wind Energy Council, Brussels, Belgium

Li S, Lamei A, Hayatdavoodi M, Wong C (2019) Concept design and analysis of wind-tracing floating offshore wind turbines. In: ASME 2019 2nd international offshore wind technical conference, ASME, November 3–6, St. Julian's, Malta, pp. 231–238. https://doi.org/10.1115/IOWTC2019-7580

MacCamy RC, Fuchs RA (1954) Wave forces on piles: a diffraction theory. Tech. Memo. No. 69, Beach Erosion Board. Army Corps of Engineers, pp 1–17

Nair BG, Vijayakumar R, Ananthakrishnan P (2019) Hydrodynamic aspects of turret-moored FPSOs. Lecture notes in civil engineering, vol 22. Springer, Singapore, pp 401–422

NumSoft Technologies (2020) HYDRAN-XR, hydrodynamic response analysis with integrated structural finite element analysis, version 20.1. Technical Report. Numsoft Technologies

Wang K, Ji C, Xue H, Tang W (2016) Frequency domain approach for the coupled analysis of floating wind turbine system. Ships Offshore Struct 5302:1–8. https://doi.org/10.1080/17445302.2016.1241365

Weiss CVC, Guanche R, Ondiviela B, Castellanos OF, Juanes J (2018) Marine renewable energy potential: a global perspective for offshore wind and wave exploitation. Energy Convers Manage 177:43–54. https://doi.org/10.1016/j.enconman.2018.09.059

Wong C (2015) Wind-tracing rotational semi-submerged raft for multiturbine wind power generation. European wind energy association offshore 2015 conference, March 10–12, Denmark, Copenhagen, pp 1–10

Zanganeh R, Thiagarajan K (2018) Prediction of the mean heading of a turret moored FPSO in bi-modal and bi-directional sea states. Appl Ocean Res 78:156–166. https://doi.org/10.1016/j.apor.2018.04.006